^{234}Th as a tracer of particulate export and remineralization in the Southeastern Tropical Pacific

Black, E.E., Buesseler, K.O, Pike, S.M., and Lam, P.J., 2018, ^{234}Th as a tracer of particulate export and remineralization in the Southeastern Tropical Pacific, Marine Chemistry, doi: 10.1016/j.marchem.2017.06.009.

Abstract

Oxygen minimum zones (OMZs) are thought to be regions of decreased carbon attenuation in the upper ocean with a biological pump that could deliver a greater percentage of exported carbon to the mesopelagic relative to surrounding waters. However, much is still unknown about carbon cycling through these zones and the areas of extreme oxygen minima (nM O_2) or oxygen deficient zones (ODZs) within the OMZs. Paired sampling for ^{234}Th (t½ ~24.1 days) and particulate organic carbon (POC) was performed along a zonal transect between 77° W and 152° W during the U.S. GEOTRACES Southeastern Tropical Pacific campaign in 2013 in order to constrain the magnitude of carbon export and remineralization through the Peruvian OMZ. POC export varied by an order of magnitude from the coast to 152° W, reflecting a decrease in POC:^{234}Th ratios (>51 μm) with distance offshore and the influence of upwelling at the coast. Modeling indicated that ^{234}Th fluxes could be underestimated at coastal stations by up to 4-fold without adjustment for the impact of upwelling, which in turn would produce much lower carbon export estimates.

Low carbon Export:NPP ratios (<0.15) at the base of the euphotic zone (Ez) in the gyre support previous findings of inefficient surface export via the biological pump in the southeastern tropical Pacific. A broad remineralization feature beginning at Ez was observed across >7500 km that resulted in, on average, 3% of the POC exported from the euphotic zone reaching 100 m below Ez. Although the highest percentages (>10%) of total exported POC at 100 m below Ez were observed in the coastal ODZ region, the observed remineralization was also most pronounced these stations. While an average of 75% of the carbon export from the euphotic zone remained at Ez +100 m in the gyre, a range of 10% to 50% was observed at ODZ stations, reflecting increased attenuation. Local subsurface minima in light transmission and maxima in fluorescence were observed in the regions of greatest remineralization at the upper ODZ boundary, suggesting that complex bacterial community dynamics play a role in increased attenuation through these zones. With ODZs and OMZs predicted to grow worldwide with climate change, these areas require further large-scale and seasonal studies to assess the permanency of these attenuation features and the impact of high Gyre and lower ODZ transfer of POC on the overall efficiency of carbon export in the Pacific.

2.1 Introduction

Oxygen minimum zones (OMZs) are permanent subsurface (50 m to 1000 m) features in the global ocean where dissolved oxygen can drop to extreme minima due a combination of weak ocean ventilation and the respiration of sinking organic matter (Karstensen et al., 2008). Oxygen deficient zones (ODZs) are defined as the regions within OMZs where oxygen levels reach near or below detection using traditional methods (O_2<1 µM, see Section 2.2.6). These ODZs are characterized by coastal upwelling, which brings nutrient rich water to the surface and creates extensive, high productivity regions (Barber et al., 2001; Fiedler et al., 1991). Although these coupled high productivity-low oxygen regions currently compose only 8% of the world's ocean area (Paulmier and Ruiz-Pino, 2009), ODZs are also one of the only regions of the ocean where nitrogen loss occurs (Codispoti et al., 2001; Lam et al., 2009) and their overlying waters boast some of the highest, non-coastal annual rates of net primary production (NPP) worldwide (Siegel et al., 2014). The Peruvian upwelling system, in particular, has tremendously productive shelf waters, supporting one of the world's largest natural fisheries (Montecino and Lange, 2009). Local marine ecosystems could be substantially impacted as changes in Earth's climate result in further expansion of the world's OMZs and ODZs (Stramma et al., 2010, 2008).

In order to predict and model the impact of global climate change on oceanic carbon and nutrient budgets, the controls on regional export via the biological pump need to be better understood. The biological pump composes the processes that transform and transport organic matter beginning with the fixation of inorganic carbon dioxide in the shallow ocean (photosynthesis) and ending with the transport to depth or remineralization of particulate organic carbon (POC) to dissolved forms (Matear and Hirst, 2003). It has been predicted that without this means of sequestration and transport of carbon to the deep ocean, the earth could see an increase in atmospheric carbon dioxide of 200 ppm (Sarmiento and Toggweiler, 1984). Sequestered POC need not reach the sediments to be removed from ocean-atmospheric interactions for millennia (Kwon et al., 2009) and so quantifying the export and remineralization of POC and nutrients in the upper 100s of meters is vital. Shallow, low oxygen zones have the potential to produce enhanced export at depth relative to more oxygenated regions of the ocean as a result of observed decreases in the attenuation of organics through OMZs (Roullier et al., 2014; Van Mooy et al., 2002).

The ^{234}Th-^{238}U disequilibrium method is one of the most established means of studying export and particle dynamics in the upper ocean over time scales of days to weeks (Bacon et al., 1996; Benitez-Nelson et al., 2001; Bhat et al., 1969; Buesseler et al., 1992; Coale and Bruland, 1987). ^{234}Th (t ½ = 24.1 days) is highly particle reactive, while its long-lived ^{238}U parent (t ½ = 4.47 billion years) behaves conservatively with respect to salinity in the ocean (Not et al., 2012; Owens et al., 2011). As a result of its long half-life and ubiquity in the ocean, ^{238}U is generally at secular equilibrium with its ^{234}Th daughter (activity ratio = 1) throughout much of the water column. In the surface ocean, a deficit between ^{234}Th and its parent is created when particles transporting ^{234}Th sink faster than new ^{234}Th is created via decay. This disequilibrium is used to calculate a particulate ^{234}Th flux. If the element:^{234}Th ratio on particles is known, the flux of the element can be found (Buesseler et al., 2006, 1992). As higher resolution profiles have become available, the ^{234}Th method has also been used to identify areas of intense remineralization just below the sunlit surface ocean (Buesseler et al., 2008; Maiti et al., 2010; Savoye et al., 2004).

Until the 2010s, the only prior ^{234}Th data from near the 12° S line came from the JGOFS equatorial Pacific program in the early 1990s (Bacon et al., 1996; Buesseler et al., 1995; Murray et al., 1996). Sampling methods for these studies varied from high volume, discrete depth pumping (Bacon et al., 1996) to drifting traps (Murray et al., 1996) to oscillating a pump over the upper 100 m to obtain an average surface value (Buesseler et al., 1995). Unlike previous studies, whose results were often limited spatially (a few locations with high sample numbers) or by a lack of depth resolution, this campaign allowed for an unprecedented look at this region's surface ocean with almost 340 total ^{234}Th samples in the upper 400 m. The data presented here reflect distinct features along the transect that might have been missed with poorer sampling resolution.

2.2 Methods

Samples were collected aboard the R/V Thomas G. Thompson between October 29th and December 18th, 2013. This cruise, the U.S. GEOTRACES Eastern Pacific Zonal Transect (GP16-TN303) will be referred to as 'the transect' here. Sampling began off the coast of Lima, Peru and continued westward to Tahiti between 10° S and 20° S. Sampling for total and particulate parameters was completed at a total of 22 stations (black squares and grey circles, Fig. 1). To increase spatial resolution, total samples were also taken at 13 additional stations in the upper 1000 m (white circles, Fig. 1). Although ^{234}Th samples were collected throughout the full water column,

data available through BCO-DMO (http://www.bco-dmo.org/dataset/643213; see Database References), the analysis presented here will focus on the upper water column only (0 to 400 m).

2.2.1 Total ^{234}Th collection and analysis

Total ^{234}Th samples were collected at 35 stations. At 'super' stations (1, 11, 18, 26, and 36) and 'full' stations (7, 9, 13, 15, 17, 20, 21, 23, 25, 28, 30, 32), 8 to 13 discrete depths were sampled through the upper 400 m (Fig. 1). At the remaining stations, 8 to 12 depths were sampled in the upper 400 m, which for shallow shelf stations covered most of the water column. A standard, 12-Niskin rosette was used to collect the total ^{234}Th samples from the upper 400 m and between 4 and 9 of the rosette depths were matched to those of in-situ pumping systems deployed on a subsequent cast to obtain particulate ^{234}Th. At a third of the stations, surface samples for total ^{234}Th were collected from the ship's underway system (~5 m below the surface) and on a few occasions 1 to 2 extra shallow depths were sampled using wire-attached Niskin bottles above in-situ pumps on later casts. Additional total samples were taken to improve the resolution of shallow features.

Total ^{234}Th analyses followed the small volume, 4 L method developed in Buesseler et al. (2001) and detailed in Owens et al. (2015). An exact 1 mL aliquot of ^{230}Th (46.34 dpm g^{-1}) was used as the yield monitor. Quartz microfiber filters (QMA) were used to collect the precipitate from the 4 L process and immediately dried. ^{234}Th measurements were made with RISO Laboratories anti-coincidence beta counters. Filters were counted twice for a minimum of 12 h at sea. As long as the calculated gross counts per minute from these 2 measurements were within 10%, they were averaged for the at-sea ^{234}Th value. The filters were counted again ~6 months later to quantify the background radioactivity due to the beta decay of long lived natural radionuclides that are also precipitated. The mean value of the at-sea counts (decay-corrected to the time of collection) minus the background value for each filter is reported here as the ^{234}Th activity (dpm L^{-1}).

In order to determine ^{234}Th activity deficits, ^{238}U activities were calculated using the salinity relationship described in Owens et al. (2011) and shown here:

$$^{238}U(\pm 0.047) = (0.0786 \pm 0.00446) * Salinity - (0.315 \pm 0.158) \quad \text{(Eq. 1)}$$

where ^{238}U activity is in dpm L^{-1}. The efficiency of the beta detectors was determined by minimizing the ^{234}Th deviation from ^{238}U for samples collected from regions of the water column

where ^{234}Th and ^{238}U are expected to be at equilibrium. These included depths below 1000 m and above 500 m off the seafloor that were not near the coastal shelf or the hydrothermal vent. For these samples (n = 93) the mean derived ^{238}U activity and standard deviation (s.d.) were 2.407 ± 0.004 dpm L^{-1}, a value well within observed natural ranges (Owens et al., 2011). High activity ^{238}U standards were measured periodically to track any changes in detector operation.

The reported ^{234}Th activities were corrected for the chemical recovery efficiency of the ^{234}Th-Mn precipitate method. To determine the percent recovery of the added ^{230}Th tracer, the method detailed in Pike et al. (2005) was followed without the initial ion exchange column chemistry steps. Filters were leached in a nitric acid-hydrogen peroxide solution and 1 gram of a ^{229}Th yield monitor (68.87 dpm g^{-1}) was added. Samples were then sonicated for 20 min, allowed to stand covered overnight, diluted, and prepared for analysis by ICP-MS. The mean chemical recovery for all samples was 90.8% with a median value of 91.6%.

2.2.2 Particulate ^{234}Th, carbon, and nitrogen collection and analysis

Particulate ^{234}Th samples were taken using dual-filter head McLane in-situ pumping systems (Bishop et al., 2012). At super stations, 3 pump casts were performed with 5 to 9 depths in the upper 400 m (black squares, Fig. 1). Pumps were deployed to capture 4 to 6 depths in the upper 400 m on 2 casts at full stations and on 1 cast at shelf stations 2 to 5 and at station 34 (grey circles, Fig. 1). The filter heads each contained a 51 µm pore size pre-filter followed by either a Supor filter or a pre-combusted and acid-leached QMA filter with a nominal pore size of 1 µm (Lam et al., 2015b). The material on the 51 µm pre-filter from the Supor filter head was rinsed onto silver filters using 0.1 µm filtered seawater and dried. The 142 mm QMA filter was oven dried and subsampled with a 25 mm punch. Both the silver filter and the 25 mm QMA subsample were counted once at sea and ~ 6 months later. The average sample volume through the 51 µm pre-filter was 404 L and for the area of the QMA subsample was 41 L. The >51 µm sample will be referred to as the large size fraction (LSF) and the 1 µm to 51 µm as the small size fraction (SSF).

Particulate organic carbon (POC) and organic nitrogen (PON) were measured after all ^{234}Th analyses were completed. The silver and 25 mm QMA were acid-fumed with concentrated HCl and then POC and PON were measured by combustion. Measurements were made on 2, 12 mm diameter punches of the QMA filters with a Flash EA1112 Carbon/Nitrogen Analyzer and using a Dynamic Flash Combustion technique. Half of the silver filters were used for POC analysis on

either a Carlo Erba 1108 or a CE Instruments NC2500 elemental analyzer interfaced to a ThermoFinnigan Delta Plus XP isotope ratio mass spectrometer. Measurements were blank corrected using dipped blanks housed near the filter heads on 1 pump from each cast. The s.d. of the blank filters was used to estimate the error in the POC and PON measurements. The SSF dip blank s.d. for the full water column was 21.8 µmolC/filter, with a maximum sample value (0 m to 500 m) of 9.4 µmolC. The SSF dip blank s.d. for nitrogen was 6.1 µmolN/filter. The LSF s.d. for carbon was 0.50 µmolC/filter and the maximum surface sample value was 3.3 µmolC. The LSF s.d. for nitrogen was 0.13 µmolN/filter.

2.2.3 Net primary production

NPP was estimated at each station using MODIS.r2014 satellite products. NPP data from a 0.017º by 0.017º region (~335 km^2) containing each station were derived with a carbon-based productivity model (CbPM, Westberry et al., 2008) by Oregon State University Ocean Productivity (http://www.science.oregonstate.edu/ocean.productivity/). An average NPP for each station was determined for the previous 16 days prior to the sampling date using a weighted average of 8-day NPP products. This time period is similar to the integrated residence time of ^{234}Th in the upper water column, which has been estimated at days to a couple weeks (Coale and Bruland, 1987; Turnewitsch et al., 2008) and provides a better time scale match for the ^{234}Th-derived export estimates than 12 h to 24 h incubations (Henson et al., 2011). The response time scale of ^{234}Th, equivalent to $1/(\lambda+k)$, accounts for both the mean life of the radioisotope ($1/\lambda$ or 24.1 days/$\log_e 2$) and scavenging (k) by particles (Turnewitsch et al., 2008). NPP was also determined for the 30 days prior to sampling and with the exception of Shelf stations 2 to 5, the 30-day NPP values did not differ from 16-day averages by >5% or 2 mmolC m^{-2} d^{-1}, on average.

2.2.4 Particulate export flux of ^{234}Th

^{234}Th activity in the surface ocean can be described as a balance between production from ^{238}U, decay, sinking flux, and transport in the following equation:

$$\frac{\partial^{234}Th}{\partial t} = {}^{238}U\lambda_{Th} - {}^{234}Th\lambda_{Th} - P + V \quad \text{(Eq. 2)}$$

where ^{234}Th is the activity of total ^{234}Th in dpm L^{-1}, ^{238}U is the salinity-derived activity of uranium, λ_{Th} is the decay constant for ^{234}Th (0.0288 day^{-1}), P is the net removal of ^{234}Th on sinking particles (dpm L^{-1} d^{-1}), and V is the sum of the advective and vertical diffusive fluxes (dpm L^{-1} d^{-1}). If a

system is at steady state, the change in activity with time is assumed to be equal to zero. In many open ocean locations, horizontal and vertical transport processes can be assumed to be negligible (<10% of total flux contribution) over the timescales relevant to the sinking flux of ^{234}Th and the uncertainties of the flux estimates (Cai et al., 2010, 2008; Savoye et al., 2004). If the steady state assumption is valid and the advective and diffusive fluxes are ignored, particulate ^{234}Th export can be determined using the following equation:

$$P_{Th\,@\,z} = \lambda_{Th} \int_0^z \left({}^{238}U - {}^{234}Th \right) dz \quad \text{(Eq. 3)}.$$

The particulate flux of ^{234}Th or P (dpm m^{-2} d^{-1}) is integrated to depth z, the base of the euphotic zone (Ez) or 100 m. It can be difficult to determine whether steady state and one-dimensional (1-D) assumptions hold true without repeated sampling campaigns to the same region or without the use of other tracers. These assumptions are discussed in more detail in Sections 2.3.5 and 2.4.1.

2.2.5 Euphotic zone

The euphotic zone, generally defined from the ocean's surface to the point in the water column where 0.1% to 1% of the flux of incident photosynthetically available radiation (PAR) is reached, is a desirable depth range of integration for surface POC export (Boyd et al., 2008; Siegel et al., 2014). In theory, Ez marks the point at which NPP goes to zero (net production = gross production − phytoplankton respiration). Above Ez, POC is created and remineralized, while below this boundary POC is only remineralized or produced by chemosynthetic pathways of much smaller magnitudes. Because PAR data were not available, the 'particle production zone' method was adopted as a euphotic zone proxy (Owens et al., 2015). Ez was determined by locating the depth where fluorescence reached 10% of its maximum (Ohnemus et al., 2016). The average particle production zone depths for all stations are referred to here as the average Ez depth. Although the variable-depth Ez is informative for looking at surface export efficiency, 100 m flux estimates for ^{234}Th and POC were also determined for comparison with prior studies.

2.2.6 Oxygen data usage and saturation calculations

Oxygen levels can directly influence community structure and zooplankton migration, indicate the extent of remineralization occurring, and will undoubtedly influence carbon and nutrient cycling (Bianchi et al., 2013; Goericke et al., 2000; Maas et al., 2014; Seibel et al., 2016). A separate Sea-Bird CTD oxygen sensor (SBE 43, limit ~ 3 µM) was deployed with the

GEOTRACES (GTC) and Ocean Data Facility (ODF) rosettes. Only the ODF data from the shallow ^{234}Th cast was used because of the observed variation in the raw oxygen sensor data from one CTD to the next and from one cast to the next (Supp. Fig. 1). In addition, only the upcast data was used due to the large difference in the response of the oxygen sensor between the up- and downcasts (Supp. Fig. 2). Upcast data also matched well with the Winkler bottle measurements (limit ~ 1 µM, Supp. Fig. 2).

Oxygen is expressed as a percent, referred to as oxygen saturation, to facilitate station to station comparison across the >7500 km transect (Ohnemus et al., 2016). Oxygen saturation values were generated using the 1-m binned ODF SBE 43 oxygen data and the Gibbs-SeaWater Oceanographic Toolbox (McDougall and Barker, 2011). The depths below the mixed layer where oxygen saturation drops rapidly to the local oxygen minimum, will be referred to as the upper oxycline. In the most offshore stations, the upper oxycline ended in a minimum of ~30% saturation, so a 30% oxygen saturation boundary was used when comparing parameters between all stations.

Similar to what was performed in Ohnemus et al. (2016) using the GTC data, the upper boundary of the oxygen deficient zone was defined as the first appearance of significant curvature in the ODF saturation data starting at the water column oxygen minimum and moving towards the surface. The gradient criterion was a 0.05% change in saturation between 3 successive 1-m data bins. In broad terms, oxygen deficient suggests levels below the limit of traditional Winkler titrations (~1 µM), but aerobic processes could still occur and nanomolar concentrations are typical in these low oxygen cores (Tiano et al., 2014). Because of the SBE and Winkler method limits, as well as the low resolution of the Winkler measurements through the base of the oxycline, we do not state an exact oxygen saturation value that marks the boundary between low oxygen and oxygen deficiency. We used the curvature criterion to define the depth of this boundary, where the oxygen sensor data definitively indicated that oxygen saturation began to change rapidly.

2.3 Results

The following section contains a brief summary of the results for total ^{234}Th, particulate ^{234}Th, NPP, and ^{234}Th flux. The results for derived parameters that required more complex assessments and calculations, including the consideration of upwelling impacts on ^{234}Th export, the estimation of ^{234}Th remineralization, and the determination of POC fluxes, are contained in the Discussion.

2.3.1 Zonal delineation

The transect was divided into 3 biogeochemical zones by Ohnemus et al. (2016), including the Shelf ODZ (stations 1 to 5, 77° W to 79.5° W), the Offshore ODZ (6 to 13, 79.5° W to 100° W), and the Gyre (14 to 36, 100° W to 152° W). Patterns in ^{234}Th deficits,^{234}Th excesses, POC:^{234}Th ratios, and NPP generally followed these zones and so the same station delineations are used here, with one exception (Fig. 1, Table 1). Stations 14 and 15 have been included in the Offshore ODZ instead of in the Gyre, making the zonal boundary 105° W. As will be discussed below, these stations did not reach oxygen deficiency, but were more similar to the Offshore ODZ stations in other biological characteristics. The zones will be referred to here as the 'Shelf', 'Offshore' and 'Gyre'.

In summary, the Shelf was dominated by microplankton (diatoms and dinoflagellates, Ohnemus et al., 2016) with an average mixed layer depth (MLD) of 21 m and an Ez of 43 m (Table 2, Supp. Table 1). The averages for the Offshore showed a >2-fold deepening of all features with a MLD of 59 m and Ez of 123 m. The Offshore boundary was moved to station 15 because pigment analysis showed a dominance of nanoplankton in the top 100 m until station 15 (Ohnemus et al., 2016) and a large contrast in SSF ^{234}Th activities was also apparent between stations 15 and 17 (Fig. 2D). Below 100 m, picoplankton dominated in the Offshore. In the Gyre, the MLD average was similar to that of the Offshore at 60 m and the average Ez was the deepest of the 3 zones at 169 m. The Gyre was dominated by picoplankton.

Oxygen saturation varied from a low of 0.2% within the ODZ at 89° W to >100% in the surface mixed layer (Fig. 2, Supp. Table 1). Saturation values were lowest in the Shelf where the average upper boundary of the ODZ was 54 ± 12 m (s.d.). The depth of minimum oxygen saturation in the Shelf was 90 ± 45 m with an average oxygen saturation value at this depth of 0.4 ± 0.1%. In the Offshore, stations to the east of 100° W (station 13) contained zones of oxygen deficiency and those to the west contained only oxygen minima. For those stations with an ODZ boundary, the average depth was 152 ± 56 m. The average depth of the oxygen minimum in the Offshore was 200 ± 85 m and the average saturation at this depth was 1.5 ± 2%. The deepest oxygen minima were found in the Gyre with an average value of 14 ± 8% and a depth of 337 ± 25 m.

2.3.2 Total and particulate ^{234}Th

Total ^{234}Th activities ranged from 0.52 dpm L^{-1} to 2.95 dpm L^{-1} for all depths sampled (Fig. 3). All stations that were occupied showed pronounced surface deficits of ^{234}Th relative to ^{238}U.

Shelf stations had the greatest surface deficits of ^{234}Th (up to 2 dpm L^{-1}) with ^{234}Th activities dropping as low as 0.5 dpm L^{-1} (Fig. 3). Although the MLD and Ez deepened with distance offshore (Supp. Table 1), ^{234}Th surface activities were remarkably consistent from 80° W. In a typical open ocean setting, ^{234}Th and ^{238}U profiles (Fig. 3) can resemble those found at Station 33 (no measureable excess ^{234}Th in the subsurface) or those at Station 9 (excess ^{234}Th in the subsurface). The Shelf profiles generally did not show an excess of ^{234}Th and reached equilibrium 10 m to 30 m below Ez, but above 100 m. The influence of upwelling on these profiles is discussed in Section 2.4.1. Subsurface excesses were observed at most other stations. The transition from deficit to excess was reached at or near Ez from the Shelf until 110° W. After 110° W and starting at station 18, Ez dropped below this transition point into the zone of excess ^{234}Th. The coincidence of Ez and the deficit-excess transition occurred again between 142° W and 152° W.

The SSF composed the majority of particulate ^{234}Th measured along the transect. The SSF ranged from 20% to 50% of the total ^{234}Th in the top 100 m and 10% to 40% between 100 m and 200 m (Fig. 2D). Almost all values above 40% for the SSF were confined to the top 50 m between 120º W and 130º W. Less than 10% of ^{234}Th total was observed to be in the LSF, except from 91.5° W to 96.5° W, where values reached 10% to 20% of the total ^{234}Th (Fig. 2E). A distinct high in the percentage of both particulate size fractions was also observable along the oxycline at the top of the ODZ in the Shelf and the Offshore regions, although it was most pronounced in the SSF. This feature also aligned with a decrease in light transmission (Fig. 2B).

2.3.3 Particulate carbon:^{234}Th and nitrogen:^{234}Th

For this study, the analysis is limited to element:^{234}Th ratios between the MLD and 400 m, the region of the water column that is relevant for ^{234}Th-derived export at Ez and subsurface remineralization calculations. In general, LSF POC:^{234}Th ratios decreased with depth and with distance offshore (Fig. 4). The highest euphotic zone ratios (non-mixed layer) were found in the Shelf, reaching >15 µmol dpm^{-1}, and in the Offshore and Gyre these ratios were <4 µmol dpm^{-1}. Below 100 m, very little change in ratios with depth was observed. The mean subsurface POC:^{234}Th was calculated for each zone by averaging all samples below Ez and above 400 m (Table 2). The Shelf average was highest at 1.4 ± 0.3 µmol dpm^{-1} (s.d.) and dropped to 0.9 ± 0.2 µmol dpm^{-1} and 0.7 ± 0.1 µmol dpm^{-1} in the Offshore and Gyre, respectively.

LSF particulate organic nitrogen (PON) to ^{234}Th showed a decrease across the transect of similar magnitude to that observed for the LSF POC: ^{234}Th (Supp. Fig. 3). Ratios decreased with depth and the maximum value measured below the MLD in the top 400 m was ~3 µmol dpm^{-1}. The subsurface (Ez to 400 m) Shelf average was highest at 0.2 ± 0.05 µmol dpm^{-1}. The averages for the Offshore and Gyre were about half at 0.10 ± 0.04 and 0.08 ± 0.03, respectively.

LSF element:^{234}Th ratios are generally used when calculating export because this fraction has been operationally defined as representative of 'sinking' particles (e.g. Bishop et al., 1977). Differences in the LSF and SSF element:^{234}Th ratios were assessed as a check on how similar sinking ratios were to suspended ones. Like the LSF, the SSF ^{234}Th ratios for both POC and PON generally decrease with depth and east to west across the transect (Table 2). In each zone, the subsurface (Ez to 400 m) average of SSF POC:^{234}Th ratios was within one standard deviation of the LSF ratio average. While the overlap of LSF and SSF POC:^{234}Th within the estimated uncertainty ensures that flux estimates using the LSF ratios are representative of all potentially sinking material, this overlap is atypical. For example, in the Gulf of Mexico pump samples taken at 120 m showed an increase from 2.8 µmol dpm^{-1} to 34.4 µmol dpm^{-1} to 124.7 µmol dpm^{-1} when going from the 10-50 µm to the 50-150 µm and to the >150 µm size fraction, respectively (Hung et al., 2010).

2.3.4 Net primary production

NPP estimates for the 16 days prior to sampling ranged from 34 mmolC m^{-2} d^{-1} to 61 mmolC m^{-2} d^{-1} in the Offshore and Gyre, while the Shelf NPP values ranged from 63 mmolC m^{-2} d^{-1} to 188 mmolC m^{-2} d^{-1} (Table 3). The highest NPP observed was at station 2 in the Shelf and the lowest was station 36, in the Gyre. NPP in the Shelf varied substantially in the month prior to sampling, dropping as low as 8 mmolC m^{-2} d^{-1} at station 3 in late October and rising to >3000 mmolC m^{-2} d^{-1} at station 2 just 8 days after. The 16-day NPP for the non-Shelf stations was very consistent at 48 ± 6 mmolC m^{-2} d^{-1} (s.d.).

Averages for the 8 days prior to sampling and annual estimates (1997 to 2008) from the SeaWIFS-based GBC14 global carbon export model (Siegel et al., 2014) have been included here for comparison (Table 3). The 8-day and annual averages for NPP were within 1 mmolC m^{-2} d^{-1} to 4 mmolC m^{-2} d^{-1} except for a few stations in the Shelf. Annual and 8-day export estimates derived with the GBC14 model were also very similar. The largest differences between the 8-day

SeaWIFS and the 16-day MODIS NPP values were seen in the Shelf and the Gyre. Despite these differences, the same general trend was observed in both datasets: higher NPP in the Shelf and the region around 140° W (Table 3). Considering all stations, the SeaWIFS 8-day NPP values were only 13% higher (and the annual only 9% higher) than the MODIS NPP estimates, on average (Table 2).

2.3.5 Particulate flux of ^{234}Th

Steady state, 1-D estimates of ^{234}Th fluxes using 100 m and Ez as integration depths produced similar results for most stations (Tables 1 and 2, Supp. Table 2). The 100 m estimate was not consistently higher or lower than the Ez-based estimate, but in the Offshore and Gyre results from both methods were within uncertainties, except for at stations 14 and 26. Including estimates derived at both depths, ^{234}Th fluxes ranged between 900 dpm m^{-2} d^{-1} and 2700 dpm m^{-2} d^{-1}. The average ^{234}Th flux at Ez for the Shelf, Offshore, and the Gyre zones was 1400 dpm m^{-2} d^{-1}, 1900 dpm m^{-2} d^{-1}, and 1600 dpm m^{-2} d^{-1}, respectively (Table 2). This consistency in ^{234}Th flux with distance offshore was unsurprising considering the observed similarities in surface deficit magnitude and depth (Fig. 2F). The average ^{234}Th flux (un-adjusted for upwelling) for the transect was 1600 dpm m^{-2} d^{-1} for both methods.

The steady state assumption for the ^{234}Th flux calculations was evaluated using the MODIS-derived NPP for each station. Between September and December, the region between 80° W and 152° W showed very little change in surface NPP. Excluding stations 2, 3, and 4, the average percent change in NPP across the transect between the 16-days prior to sampling and the previous 16 days was 1 ± 13%. While variations in NPP cannot be directly related to changes in ^{234}Th activities over the same time period, the negligible change in NPP suggested that the Offshore and Gyre regions were not experiencing a significant bloom that could have impacted ^{234}Th activities and that a steady state model was sufficient. The Shelf stations 2, 3, and 4 (77° W to 78° W), on the other hand, showed a larger change in NPP between these 16 day periods, with increases of ~760%, 410%, and 130%. Coastal zones are notoriously difficult for quantifying spatial and temporal changes in NPP and export, especially with satellite-derived data (Saba et al., 2011). The observed swings in progressive 8-day NPP estimates for these 3 stations are evidence of the challenges inherent in estimating NPP for coastal regions. For example, between late October and the end of December the average NPP at station 2 was 130 mmolC m^{-2} d^{-1} with a s.d. of almost 90

mmolC m^{-2} d^{-1}. Due to the lack of in-situ NPP and temporal ^{234}Th data along this 1° of longitude, we do not attempt to constrain the potential temporal variability in ^{234}Th distributions, and assume steady state.

2.4 Discussion

2.4.1 Influence of upwelling and horizontal advection on ^{234}Th export estimates

Prior ^{234}Th, Beryllium-7, and helium studies off Peru indicated that upwelling could substantially impact the ^{234}Th activity balance at coastal stations (Haskell et al., 2015, 2013; Steinfeldt et al., 2015). If physical factors are taken into account, particulate ^{234}Th flux is calculated as follows:

$$P_{Th\,@\,z} = \int_0^z \left(\lambda_{Th}\left({}^{238}U - {}^{234}Th\right) \pm w\frac{\partial {}^{234}Th}{\partial z} \pm u\frac{\partial {}^{234}Th}{\partial x} \pm v\frac{\partial {}^{234}Th}{\partial y} \right) dz \quad \text{(Eq. 4)}$$

where *w* is the upwelling velocity, *u* is the zonal velocity, and *v* is the meridional velocity. The gradients (∂^{234}Th terms) are vertical (with depth), west to east, and south to north, respectively.

The impact of east-west horizontal advection on ^{234}Th fluxes during the month prior to sampling was determined to be negligible based on calculated ^{234}Th surface gradients and average zonal (*u*) and meridional (*v*) geostrophic current velocities (Supp. Fig. 4). The east-west gradient in average ^{234}Th activities for a 30 m surface layer across the transect was considered (Brink et al., 1983). No significant horizontal gradient was observed between 89° W and 152° W, but a gradient of 3.5×10^{-7} dpm L^{-1} m^{-1} was observed between 89° W and the Peruvian coast. Monthly satellite-derived surface currents for October, were examined along 12° S (0.5° by 0.5° scale). Although the absolute zonal and meridional velocities reached maxima of 0.09 m s^{-1} and 0.19 m s^{-1}, respectively, the cumulative (taking into account direction) average velocities observed across this area were <0.008 m s^{-1}. This suggested that a consistent pattern in surface currents did not exist in the region and would not affect ^{234}Th gradients. However, if the east-west coastal gradient of 3.5×10^{-7} dpm L^{-1} m^{-1} was applied to a maximum current velocity of ~0.2 m s^{-1}, the result would be a meager 180 dpm m^{-2} d^{-1} change in ^{234}Th flux calculated at Ez. In this extreme case, the zonal horizontal advection term in Eq. 4 would only total 11% of the average ^{234}Th flux from Ez for stations between 89° W and the coast (Table 1). Therefore, the horizontal advection terms in Eq. 4 were disregarded.

Previous ^{234}Th modeling of the equatorial Pacific suggests that the influence of upwelling in the region between 95° W to 140° W (10° S to 15° S) should be negligible (w<0.5 m d^{-1}; Buesseler et al., 1995), but prior ^{7}Be-, temperature-, and helium-derived upwelling rates for coastal waters between 78° W to 85° W (10° S to 15° S) can vary from 0 m d^{-1} to 3 m d^{-1} (Haskell et al., 2015; Steinfeldt et al., 2015). Total ^{234}Th distributions and curved isohalines and isopycnals in the upper 100 m of the Shelf indicated some degree of upwelling (Supp. Figs. 5 and 6). The following simplification of Eq. 4 can be used to determine the particulate ^{234}Th flux adjusted for the impact of upwelling, assuming that any upwelled waters reaching the surface contained ^{234}Th at equilibrium with ^{238}U:

$$P_{Th\,@\,z} = \int_0^z \left(\lambda_{Th}\left({}^{238}U - {}^{234}Th \right) + w\frac{\partial\, {}^{234}Th}{\partial z} \right) dz \qquad \text{(Eq. 5)}$$

Based on equilibrium activities observed from 100 m to 200 m in the Shelf zone (Figs. 2F and 3), this assumption is valid if the upwelled waters originate locally. Stations in the Offshore could have been supplied with upwelled waters containing an excess of ^{234}Th, which would lead to slightly conservative estimates of upwelling-adjusted fluxes. However, it will be shown that the impact of upwelling on Offshore stations was substantially less than in the Shelf, with only two stations showing any distinguishable gradient of ^{234}Th with depth in surface waters.

Both a vertical gradient ($\partial^{234}Th/\partial z$) and upwelling rate ($w$) are needed to determine the upwelling component of ^{234}Th flux in Eq. 5. The gradient was determined at each station using 3 to 8 sampling depths beginning at the base of the mixed layer. The number of sample points used depended on the sampling resolution at that station and the depth extent of the gradient. The termination of the gradient often coincided with a change in the curvature (slope) of the ^{234}Th profiles (Fig. 3, Supp. Table 3) and was often at or just below the depth of equilibrium between ^{234}Th and ^{238}U. The depth where the ^{234}Th gradient terminated also occurred very close to the depth where large surface gradients in potential density stabilized near 1026.2 kg m^{-3} (density difference between 1 m sampling bins dropped below 0.025 for at least 40 m, Supp. Fig. 6). Gradients were calculated for all stations, so as to provide a range for the typical gradients that could exist in areas without upwelling. Much larger gradients in ^{234}Th with depth were observed at stations 1 to 7, with an average value of 0.04 ± 0.02 dpm L^{-1} m^{-1} (s.d.). In comparison, the average calculated for stations 8 to 36 was 0.009 ± 0.002 dpm L^{-1} m^{-1}. Stations 8 and 9 had ^{234}Th gradients that were

indistinguishable (± 0.002) from those found in the far western part of the transect. Therefore, Eq. 5 was used to calculate upwelling-adjusted fluxes for stations 1 through 7 and ^{234}Th fluxes for the remaining stations west of 85º W (8 to 36) were calculated using Eq. 3 only.

Using data collected during this campaign and paired ^{7}Be-temperature modeling, Kadko (2017) determined upwelling rates for six stations located between 79° W and 104° W (Supp. Table 3). Kadko (2017) and other prior studies (Haskell et al., 2015; Kadko and Johns, 2011) determine upwelling rates using the dilution of the ^{7}Be inventory in the surface ocean by upwelling of ^{7}Be-free waters from below. ^{7}Be-derived upwelling rates are well suited for use with ^{234}Th because of the comparable half-life (~53 days) and ^{7}Be-derived rates will reflect trends observed over a greater portion of the euphotic zone than tracers like helium (Haskell et al., 2015). A 1-D model was used by Kadko (2017) to determine the ^{7}Be-derived upwelling rate at the base of the mixed layer for cases of invariant upwelling with depth (singular, constant value) and depth-dependent upwelling (linear decrease of upwelling rate with depth).

To determine upwelling-adjusted ^{234}Th fluxes for stations 1 to 7 (77° W and 84° W), station-specific ^{234}Th gradients ($\partial^{234}Th/\partial z$, Supp. Table 3) were paired with the appropriate upwelling rates (w) from Kadko (2017) using Eq. 5 for the depths over which a gradient existed (Supp. Table 3, Fig. 3). For the depth region above and below this gradient zone, which included the mixed layer, the w and $\partial^{234}Th/\partial z$ terms were set to zero. While ^{234}Th gradients are available for all stations between 77° W and 84° W, upwelling rates (constant model, CM; 0 m s^{-1} horizontal advection, 0HA) were only determined by Kadko (2017) for stations 1 at 79.2° W (3.0 m d^{-1}) and 7 at 84° W (1.1 m d^{-1}). These w were used at stations 1 and 7; at coastal stations 2 through 5, the w from station 1 was applied; and at station 6, located approximately halfway between station 1 and 7, the average w from these surrounding stations was used (Supp. Table 3). The constant model results were utilized because the upwelling structure was unknown and the w values converged near Ez, where Kadko (2017) suggested that model choice was relatively unimportant.

To assess the uncertainties in the w values, at any chosen depth the flux component due to upwelling was determined for both the constant and depth-dependent models, for horizontal advection of 0 m s^{-1} to 2 m s^{-1}, and for the range of w shown in Supp. Table 3. Although it was determined that horizontal advection would not impact ^{234}Th surface fluxes significantly, a 0.1 m s^{-1} horizontal advection term is consistent with historical results and ^{7}Be, which with a half-life

more than double that of ^{234}Th, has the potential to be affected by physical factors over longer time scales. The range in the upwelling component of ^{234}Th flux, as calculated using all of these cases (vertical lines, Supp. Fig. 7), was used as the uncertainty on the CM0HA results (open circles, Supp. Fig. 7) which are summarized in Supp. Table 3.

Upwelling adjustments raised fluxes at the stations between the Peruvian coast and 84º W by an average of 2500 dpm m^{-2} d^{-1} or ~175% (Supp. Table 3). Figure 5 shows the original ^{234}Th flux estimates (black bars) with the added upwelling component (white bars), the sum of which is equivalent to the total ^{234}Th flux at Ez. Values in the 3000 dpm m^{-2} d^{-1} to 6000 dpm m^{-2} d^{-1} range have also been seen in the Equatorial Pacific, the Southern Ocean, and the Arabian Sea (Buesseler et al., 2001a, 1998, 1995). Similar ^{234}Th flux increases (1 to 5 times) due to upwelling were also observed near Hawaii (w = 1 to 3 m d^{-1}; Maiti et al., 2008). Even with conservative uncertainty estimates on the upwelling component of ^{234}Th flux at Ez, which approached 50% at many of the coastal stations (Fig. 5, Supp. Fig. 7), the impact of upwelling on ^{234}Th surface activities and fluxes was significant and should be accounted for when performing similar studies in this region.

2.4.2 Upper ocean remineralization of ^{234}Th and particle cycling

The processes composing the biological pump result in a net transport of particulate ^{234}Th from surface waters and a ^{234}Th deficit above Ez. Below Ez, any process that attenuates flux or transfers sinking particles containing ^{234}Th to suspended particles, results in an excess in total ^{234}Th. Without high resolution ^{234}Th profiles, however, the signature of these particle remineralization processes are often missed (Maiti et al., 2010). Remineralization may be occurring but not observed if the majority of it occurs over a narrow depth zone within the water column that is not sampled, or if the rates are too slow over a large depth zone within the water column for the signal to be captured within the time scale of the ^{234}Th method.

The extensive sampling along the transect captured a defined remineralization feature in the first 200 m below Ez at 27 of the 35 stations where total ^{234}Th was measured (Fig. 3, Table 1). With changing Ez, remineralization is best compared by looking at the first 100 m below Ez, where flux attenuation is largest (Buesseler and Boyd, 2009). The decrease in ^{234}Th flux was calculated between the Ez and 100 m below it (R_{100}) and from 100 m below Ez to 200 m below Ez (R_{200}). After upwelling-adjustments were made, 9 of 10 stations in the Offshore region had identifiable remineralization features, while these features were only seen in the Gyre at 15 of 20 stations.

Some of the Shelf stations had no discernable remineralization features before or after upwelling-adjustments (1 and 2) and in the cases of stations 3, 4, and 5, ^{234}Th flux was still increasing through the Ez (Supp. Table 3). Remineralization was more difficult to assess here due to the shallow depth, condensed vertical profiles, and offset of Ez from deeper ^{234}Th-^{238}U equilibrium depths.

The average R_{100} across the entire transect was 400 ± 200 dpm m^{-2} d^{-1} (s.d.). R_{100} was highest in the Offshore with an average decrease in flux of 600 dpm m^{-2} d^{-1}. In the Gyre, the R_{100} dropped to an average of 400 dpm m^{-2} d^{-1}. If R_{200} is considered, the mean values for the Offshore and Gyre were indistinguishable and averaged between 400 dpm m^{-2} d^{-1} and 500 dpm m^{-2} d^{-1}. An increase in relative uncertainties between R_{100} and R_{200} values is apparent in Table 1. This increase in uncertainties is inherent in flux with depth calculations (Supp. Fig. 8E) and is not due to any change in the uncertainty on the total ^{234}Th measurements themselves (Coale and Bruland, 1987). For those stations which had remineralization features, ^{234}Th flux decreased on average by 30% between Ez and 100 m below it, and 60% between Ez and 200 m below it (sum of R_{100} and R_{200}).

In general, remineralization features were broad (10s to 100s of m, Fig. 2F). Remineralization features in the Offshore in particular appeared to penetrate to almost 400 m at some stations (Figs. 2F and 3). Peaks this broad are not unheard of as ^{234}Th excesses attributed to remineralization observed in the Southern Ocean have reached 400 m to 500 m (Savoye et al., 2004), but the consistency in the magnitude of R_{100} and R_{200} across these zones is atypical for a basin-scale transect, especially in a gyre (Owens et al., 2015). Although ^{234}Th-derived remineralization has been quantified by a few other studies in the Weddell Sea (Usbeck et al., 2002), Northwest Pacific (Maiti et al., 2010) and the Southern Ocean (Savoye et al., 2004), flux attention has been assessed most often relative to carbon and nutrient losses, which are covered in more detail in Sections 2.4.4 and 2.4.5.

Further insight was gained by comparing ^{234}Th flux at a given depth with the distribution of ^{234}Th between the three measured phases (total, SSF, LSF) and expressing all parameters relative to the depth where oxygen saturation first reached 30% in the surface ocean (Supp. Fig. 8). Typical open ocean profiles here (Supp. Figs. 8D and 8E), have low total ^{234}Th and elevated particulate ^{234}Th in the surface ocean due to scavenging. Particles originating in the surface ocean, where photoautotrophic primary productivity is high, scavenge ^{234}Th and transport it deeper into the water column. As particles sink and are remineralized, a decrease in particulate ^{234}Th and an

increase in dissolved ^{234}Th is expected. A local excess of ^{234}Th over its ^{238}U parent is created as many sinking particles become suspended or dissolved. These excess ^{234}Th features represent a decrease in flux with depth because less ^{234}Th will be reaching farther into the water column. This pattern was observed in most of the Gyre stations (last panel, Supp. Figs. 8D and 8E). The location of the subsurface ^{234}Th excess, when present, coincided with a drop in particulate ^{234}Th.

The particulate activity profiles for both size fractions in the Shelf and Offshore did not follow those in the Gyre (Supp. Figs. 8A to 8C) as most stations showed a distinct peak in both size fractions that began below the 30% oxygen saturation point (at or just below the upper boundary of the ODZ, Figs. 2D and 2E). These particulate peaks sometimes coincided with remineralization features (decreases in flux, Supp. Fig. 8A) but often the peak in ^{234}Th flux and subsequent drop in flux occurred well above the local subsurface particle maxima (Supp. Fig. 8C). These particulate peaks were especially pronounced in the SSF and were located progressively deeper in the water column from stations 7 to 13 (84° W to 99° W). These peaks also coincided with a decrease in light transmission and an increase in fluorescence (Fig. 2). Prior studies in this region could have missed the subsurface local maxima in particulate ^{234}Th with poorer resolution.

Oxygen deficient zones have been shown to be unique hotspots of microbial processes and particulate features. The coincidence of nitrate minima, nitrite maxima, intermediate nephloid layers, and enhanced microbial activity in the low oxygen zones of Peru and the Arabian Sea are well established (Morrison et al., 1999; Naqvi et al., 1993), although the impact of these boundaries on the particle cycling within the ODZs is not. Studies of the southeastern Pacific and the Arabian Sea have observed similar features in light transmission or backscatter in the core of the ODZ (Garfield et al., 1983; Kullenberg, 1982; Naqvi et al., 1993; Spinrad et al., 1989; Whitmire et al., 2009). A few of these studies have linked these trends to bacterial abundance and denitrification (Morrison et al., 1999; Naqvi et al., 1993). A bacterial origin is the favored explanation for these observed particle layers over inorganic origins because the features only exist at the top of the ODZ and not throughout the entire zone. In addition, Stevens and Ulloa (2008) determined that the bacterial richness, or the number of different species in the OMZ, was higher in the upper ODZ region than the richness determined for the oxic surface and deeper oxycline (across the lower boundary of the ODZ). The prokaryotic nature of the upper ODZ in the Shelf and Offshore regions of this transect have been discussed in more detail in Ohnemus et al. (2016), but in summary, their

analysis suggested the presence of both denitrifying prokaryotes and autotrophic communities near the upper ODZ boundary.

The co-occurrence of subsurface, local minima in light transmission with maxima in particulate ^{234}Th and fluorescence along the transect suggested that these bacterial communities and their metabolic products have a strong impact on particle cycling and particle reactive metals, such as thorium, in the upper Peruvian ODZ (Fig 2, Supp. Fig. 8). The net signal in ^{234}Th through the top of the ODZ was remineralization, as shown by an excess in total ^{234}Th and a decrease in flux (Fig. 2E, Supp. Fig. 8). Therefore, if the system was 1-D, particles from the surface ocean must have been stopped, slowed down with respect to sinking, and/or degraded in this zone, transferring ^{234}Th to a dissolved or non-sinking pool. However, the higher particulate activities suggest that ^{234}Th may also be scavenged onto new particles being produced below the upper boundary of the ODZ (likely by some combination of photoautotrophic and chemoautotrophic processes).

Bacteria have been shown to be important agents for trace element scavenging (Cowen and Bruland, 1985). The particulate iron measured through the upper ODZ was composed mostly of Fe(III) in the form of high-surface-area Fe(III) oxyhydroxides (Heller et al., 2017). Without additional information, it is unclear whether denitrifying bacteria, which have been shown to form metal crusts when reducing nitrate (production of nitrite resulting in Fe-II oxidation), are creating these iron oxyhydroxides (Klueglein et al., 2014). However, the Fe(III) oxyhydroxides have the potential to scavenge ^{234}Th, which would lead to a retention of ^{234}Th in the upper ODZ region of the Shelf and Offshore.

The data presented here suggest that the subsurface remineralization features captured by the ^{234}Th-method could be largely driven by anaerobic denitrification processes up to station 9 or 10 (~90° W) and aerobic respiration west of station 10. The observed subsurface excesses of total ^{234}Th, which represent a switch between net production and net respiration in the water column, consistently began at the upper ODZ boundary until station 11, where the boundary dropped to almost 200 m (Figs. 2 and 3). Secondary, deep chlorophyll maxima were only present within the ODZ up to station 10 and for the remaining stations only a single, shallow chlorophyll maximum was observed. The large remineralization features observed up to station 10 appeared to be linked to the coexistence of both denitrifying and autotrophic communities (Ohnemus et al., 2016), which are tied to the presence of ‘anaerobic’ conditions and the depth of ‘anaerobic’ conditions (light

levels), respectively. The ODZ was present at stations 11, 12, and 13, but the depth of the upper ODZ boundary was much deeper than 150 m. This suggested that a complex community structure is necessary to create the 'concentrated' remineralization feature directly below the upper ODZ boundary. In addition, the ^{234}Th activity profiles (Fig. 3) for stations 12 and 13 showed double remineralization peaks, with local maxima in excess ^{234}Th above and below the upper ODZ boundary. These double peak stations may represent a transition zone where both aerobic and anaerobic processes contributed to total remineralization.

2.4.3 Regional trends in POC:^{234}Th and PON:^{234}Th

To determine macronutrient (e.g. nitrogen) or micronutrient trace metal (e.g. iron) export at a given depth the particulate concentration ratio of that element to ^{234}Th activity measured in the LSF (>51 um) at that depth is used to calculate the particulate flux with the following relationship:

$$Element\ Particulate\ Flux\ = \frac{[Element]}{^{234}Th} * Particulate\ Flux\ ^{234}Th \quad \text{(Eq. 6)}$$

The major assumption in this empirical approach is that the element:^{234}Th ratio measured at the depth of interest is representative of the sinking particles at this depth (Buesseler et al., 2006). Eq. 6 can be used to calculate an increase or decrease in flux that might result from production or remineralization processes. Samples above the MLD were excluded from POC:^{234}Th-depth relationships (Fig. 4). Mixed layer POC:^{234}Th in the same location can vary by orders of magnitude relative to those in the underlying euphotic zone (Buesseler et al., 2009; Passow et al., 2006).

Unlike the North Atlantic GEOTRACES dataset (Owens et al., 2015), the marked decline in POC:^{234}Th ratios with longitude and the shift in Ez along the transect (Tables 1 and 2) warrant the use of regional estimates of particulate ratios. The distinct shift across the transect in both the Ez and subsurface LSF POC:^{234}Th averages can be seen in Fig. 4. Linear regressions are shown for the euphotic zones, where ratios decline sharply with depth. Vertical averages were used below Ez to 400 m because little variability in ratios was observed. These linear equations and subsurface vertical averages were used to determine the POC: ^{234}Th at any depth along the transect, not just those where particulate ^{234}Th was sampled. For example, to determine the POC flux at Ez for a given station, the (upwelling-adjusted) ^{234}Th flux was multiplied by the POC:^{234}Th at the Ez depth using the particulate ratio from one of the zones as described in Eq. 6. POC:^{234}Th uncertainties for each depth and zone represent one standard deviation as shown in Fig. 4.

2.4.4 Upper ocean export and remineralization of POC

With remarkable consistency in ^{234}Th export, calculated carbon fluxes primarily reflected the observed decrease in POC:^{234}Th across the transect, modified by the increase in ^{234}Th flux in the coastal stations due to upwelling. The average Shelf POC export at Ez reached 42 ± 27 mmolC m^{-2} d^{-1} (s.d.) while the Offshore and Gyre POC export totaled only 3 ± 2 and 1.1 ± 0.2 mmolC m^{-2} d^{-1} (Table 2). Within a given zone, the range in export and s.d. reflected the variability in POC:^{234}Th ratios (Table 3, Fig. 4). In the Offshore and Gyre, POC:^{234}Th ratios at the Ez depth were relatively consistent, so small variations in Ez did not lead to large changes in carbon flux. The Shelf stations, on the other hand, showed a linear decrease in POC:^{234}Th from the shallowest Ez at 25 m to the deepest at 66 m and so stations with deeper Ez had lower POC flux. POC export differed greatly in the Shelf and the Gyre when using Ez or 100 m as the integration depth (Table 1 and Supp. Table 2). POC export in the Shelf was underestimated by up to a factor of 8 if 100 m was used instead of Ez. This supports the move to use the variable Ez as the export reference depth of choice for comparing export efficiencies (Buesseler and Boyd, 2009; Siegel et al., 2014).

Most of the prior carbon flux studies from this region were located in the Gyre (black, Fig. 6) and reported relatively similar export values to those calculated here (blue, Fig. 6). Austral spring POC fluxes from ^{234}Th in-situ pumping efforts at 12º S were determined to be between 2.5 mmolC m^{-2} d^{-1} and 3 mmolC m^{-2} d^{-1} for 112.5º W and 2 mmolC m^{-2} d^{-1} and 2.5 mmolC m^{-2} d^{-1} for 142.5º W (Buesseler et al., 1995). The paucity of ^{234}Th-derived export values for this region and others worldwide has been and will continue to be improved by past and future GEOTRACES campaigns. However, more work is needed to not only fill in the gaps in the world's ocean where no data exists (Fig. 6), but to improve coverage throughout all seasons and to obtain more export values calculated at Ez.

Carbon remineralization was calculated in the same manner as carbon export: the decrease in ^{234}Th flux below Ez was multiplied by the POC:^{234}Th ratio for that depth (Table 3). POC remineralization was examined in the 100 m below Ez and in the subsequent 100 m (Ez + 100 to Ez + 200). POC remineralization values had rather large uncertainties due to the lack of change in the POC:^{234}Th ratios at these depths and increasing uncertainties on the ^{234}Th fluxes with depth. In the first 100 m below Ez, carbon flux decreased by a maximum of 66 mmolC m^{-2} d^{-1} (Shelf) and a minimum of 0.1 mmolC m^{-2} d^{-1} (Gyre), showing a much larger gradient in remineralization

in the 100 m below Ez relative to ^{234}Th. In the next 100 m, from Ez +100 to Ez + 200, the decrease in flux was relatively small outside the Shelf (maximum 10 mmolC m^{-2} d^{-1} decrease), ranging from only 0.1 mmolC m^{-2} d^{-1} to 0.8 mmolC m^{-2} d^{-1}. The concept that POC attenuation, in general, is greatest at shallow depths has long been established in prior studies and enforces the concept of using Ez-based interpretation to compare studies (Buesseler and Boyd, 2009).

2.4.5 Strength and export efficiency of the regional biological pump

The fraction of surface production (NPP) that makes it out of the euphotic zone is often referred to as the strength of the biological pump, whereas the export efficiency of the biological pump refers to the fraction that is not remineralized in the twilight zone (Ez to ~1000 m, Buesseler and Boyd, 2009). Some studies have predicted that the strength and export efficiency of the biological pump will decrease as the global climate changes, leading to increased atmospheric levels of carbon dioxide (Manizza et al., 2010; Steinacher et al., 2010). We have assessed the biological carbon pump along the transect relative to two parameters, Ez-ratio and T_{100}, that incorporate estimates of surface production, export, and remineralization. The Ez-ratio, defined as the POC flux at the Ez (export) divided by NPP, is an important parameter for characterizing the strength of the biological pump, or how much carbon makes it out of the sunlit upper ocean (Tables 2 and 3; Buesseler and Boyd, 2009). A large Ez-ratio for an area with low productivity would mean greater POC transport to depth than an area with moderate productivity, but a low Ez-ratio. Buesseler and Boyd (2009) also parameterized POC remineralization by relating the POC flux at 100 m below Ez to the POC flux at Ez. This parameter, T_{100}, was chosen as the depth interval of maximum POC flux attenuation. These metrics were combined (Fig. 7) to illustrate the flow of carbon through the surface biological pump and to facilitate the comparison with other studies. If the Ez-ratio is multiplied by T_{100}, the resulting value is the percentage of carbon reaching 100 m below Ez relative to what was produced in the euphotic zone (1% and 10% contours, Fig. 7).

MODIS-derived 16-day NPP for the Offshore and Gyre were within ~20 mmolC m^{-2} d^{-1} of the SeaWIFS-based 8-day and annual average NPP, while Shelf NPP values could differ by up to ~74 mmolC m^{-2} d^{-1} (Table 2 and 3). This large difference in the Shelf suggests that the coastal region is very dynamic and seasonal factors could greatly influence the productivity in this region. Prior studies of primary production in the southeastern tropical Pacific have shown similar results, where the Offshore and Gyre had lower, but consistent productivity throughout the year and the eutrophic

coastal areas showed strong seasonality (Pennington et al., 2006). If the 16-day NPP values for the Offshore and Gyre (34−61 mmolC m^{-2} d^{-1}) are considered relative to other locations worldwide (Fig. 7), they fall in between the low values observed at ALOHA (central North Pacific, ~17 mmolC m^{-2} d^{-1}) and the >100 mmolC m^{-2} d^{-1} NPP values observed in the Southern Ocean (SO) and Equatorial Pacific (EqPac). The coastal Shelf stations have comparable NPP values to locations under bloom conditions in the Southern Ocean and the North Atlantic (Natl).

Although NPP was higher in the Shelf relative to the Offshore and Gyre, POC export at Ez varied substantially from the Shelf to the Gyre, creating an order of magnitude difference in the estimated strength or Ez-ratio of the local biological carbon pump (Fig. 7). Stations in the Shelf had Ez-ratios (NPP/Export at Ez) varying from 0.5 to 0.1, while Ez-ratios in the Offshore and Gyre zones were more consistent and lower (Table 3). Average Ez-ratios in the Offshore and Gyre were 0.06 ± 0.04 (s.d.) and 0.02 ± 0.005, respectively. While up to 50% of carbon produced in the surface waters of the Shelf reached the base of the euphotic, the Offshore and Gyre saw <15% exported at all stations (Table 3). Ez-ratios under 0.1 are relatively low compared to those found in productive regions like the North Atlantic and Northwestern Pacific, but are similar to those found at other low-export Pacific sites like Station Papa (Spring), ALOHA, and the Equatorial Pacific, where <10% of POC is exported out of the euphotic zone (Fig. 7; Buesseler and Boyd, 2009). The GBC14 global export model, a food-web based model utilizing SeaWIFS satellite products, produces similar Ez-ratios in the Offshore and Gyre, with all estimated Ez-ratios under 0.2 for these regions and a consistent Ez-ratio for the Shelf stations of 0.2 (Siegel et al., 2014).

Carbon transfer ratios for the first 100 m below Ez (T_{100}) were larger, on average, in the Gyre at 0.8 ± 0.1 (s.d.), compared to the Offshore zone at 0.6 ± 0.2 and the Shelf zone at 0.4 ± 0.4 (Tables 2 and 3). This suggests lower remineralization of sinking POC in the Gyre relative to the Shelf and Offshore regions at depths just below Ez (Fig. 7). The T_{100} values for this transect cover the entire range of measured T_{100} reported for other locations worldwide in Buesseler and Boyd (2009). Most of this variability in T_{100} was observed in the Offshore zone, as the Gyre stations had consistently high T_{100} values.

Based on these results from austral spring, the 10° S to 15° S region of the southeastern tropical Pacific has a strong coastal biological pump (higher Ez-ratio), but one that has high POC flux attenuation below the euphotic zone (low T_{100}, Fig. 7). The biological pump of the Gyre, as

expected from other Pacific studies, is relatively weak but has little POC flux attenuation below the euphotic zone (Buesseler and Boyd, 2009). The Offshore biological pump, surprisingly, was consistently poor in strength but had transfer efficiencies that ranged from 0.1 to 0.9. On average, the amount of POC exported at 100 m below Ez was similar between the Offshore at 3 ± 2% and the Gyre at 2 ± 0.3% (Table 2), although it ranged from 0.4% (station 9) to 7% (station 14) in the Offshore. While there was a large spread in the data, almost all the stations from this study and prior studies fall within the 1% to 10% range for the amount of POC exported at 100 m below Ez. The percent of POC sequestered 100 m below Ez reaches a similar value at all stations by a combination of high export from the euphotic zone and rapid POC attenuation in the Shelf (shallowest Ez), progressively less export and less attenuation in the Offshore zone, and low export combined with less POC flux attenuation in the Gyre zone (deepest Ez).

While none of the stations from this study had POC export at 100 m below Ez close to the values seen at NABE (North Atlantic Bloom Experiment) or in the Southern Ocean, a 1% to 13% difference in export at this depth is not trivial if a large region of the ocean is impacted. The decrease in carbon attenuation below Ez in the Gyre zone is expected, as enhanced export through similar low oxygen regions has been shown (Roullier et al., 2014; Van Mooy et al., 2002). With expanding low oxygen regions worldwide, this trend of decreased attenuation through OMZs could lead to decreased POC export to depth over 8% of the world ocean (Paulmier and Ruiz-Pino, 2009; Stramma et al., 2008). However, further study is needed to determine the cause of the relatively low transfer efficiency for some of the Shelf and Offshore stations and whether oxygen deficient zones indeed show greater attenuation of POC relative to zones of low oxygen. Station 9 (bottom left-most point in Fig. 7), in particular, had substantially more remineralization than any of the other stations in the Offshore region. Stations 6 to 10, the only Offshore locations with deep chlorophyll maxima at or below the upper ODZ boundary, had an average T_{100} of 0.4. The remaining stations (11 to 15) in the Offshore zone, those that did not show signs of deep, light adapted autotrophs, had an average T_{100} of 0.8. This suggests that the community structure through the upper oxycline and ODZ could play an important role in controlling the percent of POC that reaches 100 m below the euphotic. The extent of this role and the degree to which ODZs have the potential to increase carbon attenuation is vital to understanding the overall effect of expanding OMZs and ODZs on the global biological carbon pump.

2.5 Conclusions

Here we have shown that the non-coastal southeastern tropical Pacific had relatively low carbon export out of the euphotic zone in the austral spring (0.8−9 mmolC m^{-2} d^{-1}), but similar Ez-ratios (Export/NPP) to other open ocean locations in the Pacific, including the productive equatorial region (Fig. 7; Buesseler and Boyd, 2009). When estimating export in coastal regions similarly influenced by upwelling, surface fluxes of carbon or other elements could be underestimated by a factor of two to four if the influence of upwelling is not account for in ^{234}Th-based estimates. Both particulate carbon and nitrogen export decreased with distance offshore, following shifts in plankton community dominance, increased Ez, and changes in POC:^{234}Th and PON:^{234}Th ratios on sinking particles. The low transfer of carbon out of the euphotic zone along the transect produced some of the lowest Ez-ratios that have been quantified worldwide (excluding the Shelf). The T_{100} values observed here were only surpassed by regions under bloom conditions. This indicated that once POC left the euphotic zone, very little was attenuated in these low oxygen regions of the ocean. Currently covering 8% of the world's ocean area, these OMZs have the potential to enhance carbon transfer to depth, especially as OMZs are predicted to expand with changing global climate (Paulmier and Ruiz-Pino, 2009). However, greater attenuation at stations through the oxygen deficient region of the OMZ (77° W to 92° W) suggests that this expansion may have a more complex effect on the regional biological carbon pump than predicted.

The upper ODZ boundary is a unique setting where further research of trace metal and nutrient cycling is warranted. Simultaneous trace metal sampling with incubation experiments, measurements of bacterial counts, and genomic studies, would help in making definitive conclusions on the metabolic capacities of local bacteria (e.g. autotrophy, nitrate reduction via denitrification, anammox), how each population impacts ^{234}Th scavenging and remineralization, and if the oxygen gradient accurately represents the relative transition from aerobic to anaerobic-dominated metabolisms. As ODZs expand worldwide, their growth may drastically impact local planktonic communities, especially those who dwell just over or under the almost anoxic boundaries (Wishner et al., 2013). ^{234}Th results suggests that these communities significantly affect subsurface particulate activities and multi-isotope analysis with longer-lived thorium isotopes (^{228}Th, ^{232}Th, ^{230}Th) could help shed light on the impact of the ODZ and its microbial communities on particle dynamics on longer time scales.

Many trace metals, like iron, have been shown to be essential for ocean microbiota and much less is known about the quantities of these metals traveling or cycling through the world's ODZs compared to that which is known about elements like carbon and nitrogen. Whereas carbon concentrations tend to follow an exponential decrease from the surface, making export calculations relatively simple, trace metals are impacted by a host of processes that can create widely different distributions metal to metal and station to station (Lamborg et al., 2008). While trace metals provide new challenges for utilizing the ^{234}Th-method, radioisotope tracers from this and other GEOTRACES cruises will provide the tools necessary to determine basin-wide, carbon, nutrient, and trace metal export flux and remineralization rates, one of the key goals of the international GEOTRACES program.

Acknowledgements

This work was supported by the National Science Foundation (OCE-1232669) and E. Black was also funded by a NASA Earth and Space Science Graduate Fellowship (NNX13AP31H). The authors would like to thank the 3 anonymous reviewers for their thoughtful comments and the captain, crew, and scientists aboard the R/V Thomas G. Thompson. Particular thanks go to the chief scientists, James Moffett and Chris German, and to the members of the pump group including Matt Charette, Willard Moore, Dan Ohnemus, and Virginie Sanial. Laboratory assistance was provided by Gretchen Swarr, Paul Henderson, Lauren Kipp, and Crystal Breier. Additional thanks goes to Kelsey Bisson and Dave Siegel who provided model-derived carbon export estimates and Dave Kadko for his ^{7}Be-derived upwelling rates.

References

Bacon, M.P., Cochran, J.K., Hirschberg, D., Hammar, T.R., Fleer, A.P., 1996. Export flux of carbon at the equator during the EqPac time-series cruises estimated from ^{234}Th measurements. Deep. Res. II 43, 1133–1153.

Barber, R.T., Marra, J., Bidigare, R.C., Codispoti, L.A., Halpern, D., Johnson, Z., Latasa, M., Goericke, R., Smith, S.L., 2001. Primary productivity and its regulation in the Arabian Sea during 1995, Deep-Sea Research II.

Benitez-Nelson, C., Buesseler, K.O., Karl, D.M., Andrews, J., 2001. A time-series study of particulate matter export in the North Pacific Subtropical Gyre based on ^{234}Th:^{238}U disequilibrium. Deep. Res. I 48, 2595–2611.

Bhat, S.G., Krishnaswamy, S., Lal, D., Rama, Moore, W.S., 1969. ^{234}Th/^{238}U ratios in the ocean. Earth Planet. Sci. Lett. 5, 483–491.

Bianchi, D., Galbraith, E.D., Carozza, D.A., Mislan, K.A.S., Stock, C.A., 2013. Intensification of open-ocean oxygen depletion by vertically migrating animals. Nat. Geosci. 6, 545–548. doi:10.1038/ngeo1837

Bishop, J.K., Edmond, J.M., Ketten, D.R., Bacon, M.P., Silker, W.B., 1977. The chemistry, biology, and vertical flux of particulate matter from the upper 400 m of the equatorial Atlantic Ocean. Deep. Res. 24, 511–548.

Bishop, J.K.B., Lam, P.J., Wood, T.J., 2012. Getting good particles: Accurate sampling of particles by large volume in-situ filtration. Limnol. Oceanogr. Methods 10, 681–710. doi:10.4319/lom.2012.10.681

Boyd, P.W., Gall, M.P., Silver, M.W., Coale, S.L., Bidigare, R.R., Bishop, J.L.K.B., 2008. Quantifying the surface-subsurface biogeochemical coupling during the VERTIGO ALOHA and K2 studies. Deep. Res. II 55, 1578–1593. doi:10.1016/j.dsr2.2008.04.010

Brink, K.H., Halpern, D., Huyer, A., Smith, R.L., 1983. The Physical Environment of the Peruvian Upwelling System. Prog. Oceanogr. 12, 285–305.

Buesseler, K.O., Andrews, J.A., Hartman, M.C., Belastock, R., Chai, F., 1995. Regional estimates of the export flux of particulate organic carbon derived from thorium-234 during the JGOFS EqPac program. Deep. Res. II 42, 777–804.

Buesseler, K.O., Bacon, M.P., Cochran, J.K., Livingston, H.D., 1992. Carbon and nitrogen export during the JGOFS North Atlantic Bloom Experiment estimated from ^{234}Th:^{238}U disequilibria. Deep. Res. 39, 1115–1137.

Buesseler, K.O., Ball, L., Andrews, J., Benitez-Nelson, C., Belastock, R., Chai, F., Chao, Y., 1998. Upper ocean export of particulate organic carbon in the Arabian Sea derived from thorium-234. Deep. Res. II 45, 2461–2487.

Buesseler, K.O., Ball, L., Andrews, J., Cochran, J.K., Hirschberg, D.J., Bacon, M.P., Fleer, A., Brzezinski, M., 2001a. Upper ocean export of particulate organic carbon and biogenic silica in the Southern Ocean along 170 W. Deep. Res. II 48, 4275–4297.

Buesseler, K.O., Benitez-Nelson, C., Rutgers van der Loeff, M., Andrews, J., Ball, L., Crossin, G., Charette, M.A., 2001b. An intercomparison of small- and large-volume techniques for thorium-234 in seawater. Mar. Chem. 74, 15–28.

Buesseler, K.O., Benitez-Nelson, C.R., Moran, S.B., Burd, A., Charette, M., Cochran, J.K., Coppola, L., Fisher, N.S., Fowler, S.W., Gardner, W.D., Guo, L.D., Gustafsson, O., Lamborg, C., Masque, P.,

Miquel, J.C., Passow, U., Santschi, P.H., Savoye, N., Stewart, G., Trull, T., 2006. An assessment of particulate organic carbon to thorium-234 ratios in the ocean and their impact on the application of ^{234}Th as a POC flux proxy. Mar. Chem. 100, 213–233. doi:10.1016/j.marchem.2005.10.013

Buesseler, K.O., Boyd, P.W., 2009. Shedding light on processes that control particle export and flux attenuation in the twilight zone of the open ocean. Limnol. Oceanogr. 54, 1210–1232.

Buesseler, K.O., Pike, S., Maiti, K., Lamborg, C.H., Siegel, D.A., Trull, T.W., 2009. Thorium-234 as a tracer of spatial, temporal and vertical variability in particle flux in the North Pacific. Deep. Res. I 56, 1143–1167. doi:10.1016/j.dsr.2009.04.001

Buesseler, K.O., Trull, T.W., Steinberg, D.K., Silver, M.W., Siegel, D.A., Saitoh, S.-I., Lamborg, C.H., Lam, P.J., Karl, D.M., Jiao, N.Z., Honda, M.C., Elskens, M., Dehairs, F., Brown, S.L., Boyd, P.W., Bishop, J.K.B., Bidigare, R.R., 2008. VERTIGO (VERtical Transport In the Global Ocean): A study of particle sources and flux attenuation in the North Pacific. Deep. Res. II 55, 1522–1539. doi:10.1016/j.dsr2.2008.04.024

Cai, P., Chen, W., Dai, M., Wan, Z., Wang, D., Li, Q., Tang, T., Lv, D., 2008. A high-resolution study of particle export in the southern South China Sea based on ^{234}Th:^{238}U disequilibrium. J. Geophys. Res. 113, 1–15. doi:10.1029/2007JC004268

Cai, P., Rutgers Van der Loeff, M., Stimac, I., Nothig, E.M., Lepore, K., Moran, S.B., 2010. Low export flux of particulate organic carbon in the central Arctic Ocean as revealed by ^{234}Th:^{238}U disequilibrium. J. Geophys. Res. Ocean. 115, 1–21. doi:10.1029/2009JC005595

Coale, K.H., Bruland, K.W., 1987. Oceanic stratified euphotic zone as elucidated by ^{234}Th:^{238}U disequilibria. Limnol. Oceanogr. 32, 189–200.

Codispoti, L.A., Brandes, J.A., Christensen, J.P., Devol, A.H., Naqvi, S.W.A., Paerl, H.W., Yoshinari, T., 2001. The oceanic fixed nitrogen and nitrous oxide budgets: Moving targets as we enter the anthropocene? Sci. Mar. 65, 85–105. doi:10.3989/scimar.2001.65s285

Cowen, J.P., Bruland, K.W., 1985. Metal deposits associated with bacteria: implications for Fe and Mn marine biogeochemistry. Deep Sea Res. 32, 253–272. doi:10.1016/0198-0149(85)90078-0

Fiedler, P.C., Philbrick, V., Chavez, F.P., 1991. Oceanic upwelling and productivity in the Eastern Tropical Pacific. Limnol. Oceanogr. 36, 1834–1850.

Garfield, P.C., Packard, T.T., Friederich, G.E., Codispoti, L.A., 1983. A subsurface particle maximum layer and enhanced microbial activity in the secondary nitrite maximum of the northeastern tropical Pacific Ocean. J. Mar. Res. 41, 747–768.

Goericke, R., Olson, R.J., Shalapyonok, A., 2000. A novel niche for Prochlorococcus sp. in low-light suboxic environments in the Arabian Sea and the Eastern Tropical North Pacific. Deep. Res. I 47, 1183–1205.

Haskell, W.Z., Berelson, W.M., Hammond, D.E., Capone, D.G., 2013. Particle sinking dynamics and POC fluxes in the Eastern Tropical South Pacific based on ^{234}Th budgets and sediment trap deployments. Deep. Res. I 81, 1–13. doi:10.1016/j.dsr.2013.07.001

Haskell, W.Z., Kadko, D., Hammond, D.E., Knapp, A.N., Prokopenko, M.G., Berelson, W.M., Capone, D.G., 2015. Upwelling velocity and eddy diffusivity from 7Be measurements used to compare vertical nutrient flux to export POC flux in the Eastern Tropical South Pacific. Mar. Chem. 168, 140–150. doi:10.1016/j.marchem.2014.10.004

Heller, M.I., Lam, P.J., Moffett, J.W., Till, C.P., Lee, J.-M., Toner, B.M., Marcus, M.A., 2017. Accumulation of Fe oxides in the Peruvian oxygen deficient zone implies non-oxygen dependent Fe oxidation. Geochim. Cosmochim. Acta 211, 174-193. doi:10.1016/j.gca.2017.05.019

Henson, S.A., Sanders, R., Madsen, E., Morris, P.J., Le Moigne, F., Quartly, G.D., 2011. A reduced estimate of the strength of the ocean's biological carbon pump. Geophys. Res. Lett. 38, 1–5. doi:10.1029/2011GL046735

Hung, C.C., Xu, C., Santschi, P.H., Zhang, S.J., Schwehr, K.A., Quigg, A., Guo, L., Gong, G.C., Pinckney, J.L., Long, R.A., Wei, C.L., 2010. Comparative evaluation of sediment trap and ^{234}Th-derived POC fluxes from the upper oligotrophic waters of the Gulf of Mexico and the subtropical northwestern Pacific Ocean. Mar. Chem. 121, 132–144. doi:10.1016/j.marchem.2010.03.011

Kadko, D., 2017. Upwelling and primary production during the U.S. GEOTRACES East Pacific Zonal Transect. Global Biogeochem. Cycles 31, 1–15. doi:10.1002/2016GB005554

Kadko, D., Johns, W., 2011. Inferring upwelling rates in the equatorial Atlantic using ^{7}Be measurements in the upper ocean. Deep. Res. I 58, 647–657. doi:10.1016/j.dsr.2011.03.004

Karstensen, J., Stramma, L., Visbeck, M., 2008. Oxygen minimum zones in the eastern tropical Atlantic and Pacific oceans. Prog. Oceanogr. 77, 331–350. doi:10.1016/j.pocean.2007.05.009

Klueglein, N., Zeitvogel, F., Stierhof, Y.D., Floetenmeyer, M., Konhauser, K.O., Kappler, A., Obst, M., 2014. Potential role of nitrite for abiotic Fe(II) oxidation and cell encrustation during nitrate reduction by denitrifying bacteria. Appl. Environ. Microbiol. 80, 1051–1061. doi:10.1128/AEM.03277-13

Kullenberg, G., 1982. A comparison of distributions of suspended matter in the Peru and Northwest African upwelling areas, in: Richards, F.A. (Ed.), Coastal Upwelling. American Geophysical Union, pp. 282–290.

Kwon, E.Y., Primeau, F., Sarmiento, J.L., 2009. The impact of remineralization depth on the air–sea carbon balance. Nat. Geosci. 2, 630–635. doi:10.1038/ngeo612

Lam, P., Lavik, G., Jensen, M.M., van de Vossenberg, J., Schmid, M., Woebken, D., Dimitri, G., Amann, R., Jetten, M.S.M., Kuypers, M.M.M., 2009. Revising the nitrogen cycle in the Peruvian oxygen minimum zone. Proc. Natl. Acad. Sci. U. S. A. 106, 4752–4757. doi:10.1073/pnas.0812444106

Lam, P.J., Twining, B.S., Jeandel, C., Roychoudhury, A., Resing, J.A., Santschi, P.H., Anderson, R.F., 2015. Methods for analyzing the concentration and speciation of major and trace elements in marine particles. Prog. Oceanogr. 133. doi:10.1016/j.pocean.2015.01.005

Lamborg, C.H., Buesseler, K.O., Lam, P.J., 2008. Sinking fluxes of minor and trace elements in the North Pacific Ocean measured during the VERTIGO program. Deep. Res. Part II Top. Stud. Oceanogr. 55, 1564–1577. doi:10.1016/j.dsr2.2008.04.012

Le Moigne, F.A.C., Henson, S.A., Sanders, R.J., Madsen, E., 2013. Global database of surface ocean particulate organic carbon export fluxes diagnosed from the ^{234}Th technique. Earth Syst. Sci. Data 5, 295–304. doi:10.5194/essd-5-295-2013

Maas, A.E., Frazar, S.L., Outram, D.M., Seibel, B.A., Wishner, K.F., 2014. Fine-scale vertical distribution of macroplankton and micronekton in the Eastern Tropical North Pacific in association with an oxygen minimum zone. J. Plankton Res. 36, 1557–1575. doi:10.1093/plankt/fbu077

Maiti, K., Benitez-Nelson, C.R., Rii, Y., Bidigare, R., 2008. The influence of a mature cyclonic eddy on particle export in the lee of Hawaii. Deep. Res. II 55, 1445–1460. doi:10.1016/j.dsr2.2008.02.008

Maiti, K., Nelson, C.R.B., Buesseler, K.O., 2010. Insights into particle formation and remineralization using the short-lived radionuclide, Thoruim-234. Geophys. Res. Lett. 37, 1–6. doi:10.1029/2010GL044063

Manizza, M., Buitenhuis, E.T., Le Quere, C., 2010. Sensitivity of global ocean biogeochemical dynamics to ecosystem structure in a future climate. Geophys. Res. Lett. 37, 1–5. doi:10.1029/2010GL043360

Matear, R.J., Hirst, A.C., 2003. Long-term changes in dissolved oxygen concentrations in the ocean caused by protracted global warming. Global Biogeochem. Cycles 17, 1–32. doi:10.1029/2002GB001997

McDougall, T.J., Barker, P.M., 2011. Getting started with TEOS-10 and the Gibbs Seawater (GSW) Oceanographic Toolbox (No. SCOR/IAPSO WG127).

Montecino, V., Lange, C.B., 2009. The Humboldt Current System: Ecosystem components and processes, fisheries, and sediment studies. Prog. Oceanogr. 83, 65–79. doi:10.1016/j.pocean.2009.07.041

Morrison, J.M., Codispoti, L.A., Smith, S.L., Wishner, K., Flagg, C., Gardner, W.D., Gaurin, S., Naqvi, S.W.A., Manghnani, V., Prosperie, L., Gundersen, J.S., 1999. The oxygen minimum zone in the Arabian Sea during 1995. Deep. Res. II 46, 1903–1931.

Murray, J.W., Young, J., Newton, J., Dunne, J., Chapin, T., Paul, B., Mccarthy, J.J., 1996. Export flux of particulate organic carbon from the central equatorial Pacific determined using a combined drifting trap-^{234}Th approach. Deep. Res. II 43, 1095–1132.

Naqvi, S.W.A., Kumar, M.D., Narvekar, P. V, De Sousa, S.N., George, M.D., D'Silva, C., 1993. An intermediate nepheloid layer associated with high microbial metabolic rates and denitrification. J. Geophys. Res. 98, 16469–16479.

Not, C., Brown, K.A., Ghaleb, B., Hillaire-Marcel, C., 2012. Conservative behavior of uranium vs. salinity in Arctic sea ice and brine. Mar. Chem. 130–131, 33–39. doi:10.1016/j.marchem.2011.12.005

Ohnemus, D.C., Rauschenberg, S., Cutter, G.A., Fitzsimmons, J.N., Sherrell, R.M., Twining, B.S., 2016. Elevated trace metal content of prokaryotic plankton communities associated with marine oxygen deficient zones. Limnol. Oceanogr. 62, 3–25. doi:10.1002/lno.10363

Owens, S.A., Buesseler, K.O., Sims, K.W.W., 2011. Re-evaluating the ^{238}U-salinity relationship in seawater: Implications for the 238U–234Th disequilibrium method. Mar. Chem. 127, 31–39. doi:10.1016/j.marchem.2011.07.005

Owens, S.A., Pike, S., Buesseler, K.O., 2015. Thorium-234 as a tracer of particle dynamics and upper ocean export in the Atlantic Ocean. Deep. Res. II 116, 42–59. doi:10.1016/j.dsr2.2014.11.010

Passow, U., Dunne, J., Murray, J.W., Balistrieri, L., Alldredge, A.L., 2006. Organic carbon to ^{234}Th ratios of marine organic matter. Mar. Chem. 100, 323–336. doi:10.1016/j.marchem.2005.10.020

Paulmier, A., Ruiz-Pino, D., 2009. Oxygen minimum zones (OMZs) in the modern ocean. Prog. Oceanogr. 80, 113–128. doi:10.1016/j.pocean.2008.08.001

Pennington, J.T., Mahoney, K.L., Kuwahara, V.S., Kolber, D.D., Calienes, R., Chavez, F.P., 2006. Primary production in the eastern tropical Pacific: A review. Prog. Oceanogr. 69, 285–317. doi:10.1016/j.pocean.2006.03.012

Pike, S.M., Buesseler, K.O., Andrews, J., Savoye, N., 2005. Quantification of ^{234}Th recovery in small volume sea water samples by inductively coupled plasma mass spectrometry. J. Radioanal. Nucl. Chem. 263, 355–360.

Roullier, F., Berline, L., Guidi, L., Durrieu De Madron, X., Picheral, M., Sciandra, A., Pesant, S., Stemmann, L., 2014. Particle size distribution and estimated carbon flux across the Arabian Sea oxygen minimum zone. Biogeosciences 11, 4541–4557. doi:10.5194/bg-11-4541-2014

Saba, V.S., Friedrichs, M.A.M., Antoine, D., Armstrong, R.A., Asanuma, I., Behrenfeld, M.J., Ciotti, A.M., Dowell, M., Hoepffner, N., Hyde, K.J.W., Ishizaka, J., Kameda, T., Marra, J., Mlin, F., Morel, A., O'Reilly, J., Scardi, M., Smith, W.O., Smyth, T.J., Tang, S., Uitz, J., Waters, K., Westberry, T.K., 2011. An evaluation of ocean color model estimates of marine primary

productivity in coastal and pelagic regions across the globe. Biogeosciences 8, 489–503. doi:10.5194/bg-8-489-2011

Sarmiento, J.L., Toggweiler, J.R., 1984. A new model for the role of the ocean in determining atmospheric PCO_2. Nature 308, 621–624.

Savoye, N., Buesseler, K.O., Cardinal, D., Dehairs, F., 2004. 234Th deficit and excess in the Southern Ocean during spring 2001: Particle export and remineralization. Geophys. Res. Lett. 31, 1–4. doi:10.1029/2004GL019744

Seibel, B.A., Schneider, J.L., Kaartvedt, S., Wishner, K.F., Daly, K.L., 2016. Hypoxia tolerance and metabolic suppression in oxygen minimum zone Euphausiids: Implications for ocean deoxygenation and biogeochemical cycles. Integr. Comp. Biol. 56, 510–523. doi:10.1093/icb/icw091

Siegel, D.A., Buesseler, K.O., Doney, S.C., Sailley, S.F., Behrenfeld, M.J., Boyd, P.W., 2014. Global assessment of ocean carbon export by combining satellite observations and food-web models. Global Biogeochem. Cycles 28, 181–196. doi:10.1002/2013GB004743

Spinrad, R.W., Glover, H., Ward, B.B., Codispoti, L.A., Kullenberg, G., 1989. Suspended particle and bacterial maxima in Peruvian coastal waters during a cold water anomaly. Deep. Res. 36, 715–733.

Steinacher, M., Joos, F., Frolicher, T.L., Bopp, L., Cadule, P., Cocco, V., Doney, S.C., Gehlen, M., Lindsay, K., Moore, J.K., Schneider, B., Segschneider, J., 2010. Projected 21st century decrease in marine productivity: a multi-model analysis. Biogeosciences 7, 979–1005.

Steinfeldt, R., Sültenfuß, J., Dengler, M., Fischer, T., Rhein, M., 2015. Coastal upwelling off Peru and Mauritania inferred from helium isotope disequilibrium. Biogeosciences 12, 7519–7533. doi:10.5194/bg-12-7519-2015

Stevens, H., Ulloa, O., 2008. Bacterial diversity in the oxygen minimum zone of the eastern tropical South Pacific. Environ. Microbiol. 10, 1244–1259. doi:10.1111/j.1462-2920.2007.01539.x

Stramma, L., Johnson, G.C., Sprintall, J., Mohrholz, V., 2008. Expanding oxygen-minimum zones in the tropical oceans. Science 320, 655–659.

Stramma, L., Schmidtko, S., Levin, L.A., Johnson, G.C., 2010. Ocean oxygen minima expansions and their biological impacts. Deep. Res. I 57, 587–595. doi:10.1016/j.dsr.2010.01.005

Tiano, L., Garcia-Robledo, E., Dalsgaard, T., Devol, A.H., Ward, B.B., Ulloa, O., Canfield, D.E., Revsbech, N.P., 2014. Oxygen distribution and aerobic respiration in the north and south eastern tropical Pacific oxygen minimum zones. Deep. Res. I 94, 173–183. doi:10.1016/j.dsr.2014.10.001

Turnewitsch, R., Reyss, J.L., Nycander, J., Waniek, J.J., Lampitt, R.S., 2008. Internal tides and sediment dynamics in the deep sea - Evidence from radioactive $^{234}Th/^{238}U$ disequilibria. Deep. Res. I 55, 1727–1747. doi:10.1016/j.dsr.2008.07.008

Usbeck, R., Rutgers Van der Loeff, M., Hoppema, M., Schlitzer, R., 2002. Shallow remineralization in the Weddell Gyre. Geochemistry Geophys. Geosystems 3, 1–18.

Van Mooy, B.A.S., Keil, R.G., Devol, A.H., 2002. Impact of suboxia on sinking particulate organic carbon: Enhanced carbon flux and preferential degradation of amino acids via denitrification. Geochim. Cosmochim. Acta 66, 457–465.

Westberry, T., Behrenfeld, M.J., Siegel, D.A., Boss, E., 2008. Carbon-based primary productivity modeling with vertically resolved photoacclimation. Global Biogeochem. Cycles 22, 1–18. doi:10.1029/2007GB003078

Whitmire, A.L., Letelier, R.M., Villagrán, V., Ulloa, O., 2009. Autonomous observations of in vivo fluorescence and particle backscattering in an oceanic oxygen minimum zone. Opt. Express 17, 21992–22004. doi:10.1117/12.190060

Wishner, K.F., Outram, D.M., Seibel, B.A., Daly, K.L., Williams, R.L., 2013. Zooplankton in the eastern tropical north Pacific: Boundary effects of oxygen minimum zone expansion. Deep Sea Res. I 79, 122–140. doi:10.1016/j.dsr.2013.05.012

Website and Database References

Buesseler, K.O., Charette, M.A., & Moore, W.S. (2017) Water-column total Th-234 and U-238 from R/V Thomas G. Thompson cruise TN303 in the Eastern Tropical Pacific in 2013 (U.S. GEOTRACES EPZT project). Biological and Chemical Oceanography Data Management Office (BCO-DMO). Version: 27 January 2017. http://www.bco-dmo.org/dataset/643213

Buesseler, K.O., Charette, M.A., & Moore, W.S. (2016) Th-234 from in-situ pumps, including large size fraction (>51 um) and small size fraction (1-51 um), from R/V Thomas G. Thompson cruise TN303 in the Eastern Tropical Pacific in 2013 (U.S. GEOTRACES EPZT project). Biological and Chemical Oceanography Data Management Office (BCO-DMO). Version: 03 June 2016. http://www.bco-dmo.org/dataset/643316

NOAA, OceanWatch Central Pacific TDS THREDDS Data Server, http://pifsc-oceanwatch.irc.noaa.gov/thredds/catalog.html, Last Access: 10 Oct 2016.

NOAA, World Ocean Atlas 2009, https://www.nodc.noaa.gov/OC5/WOA09/pr_woa09.html, Last Access: 10 Oct 2016.

Ocean Productivity, Oregon State University, http://www.science.oregonstate.edu/ocean.productivity/, Last Access: 07 June 2017.

Table 1: Summary of ^{234}Th results by station including ^{234}Th-derived parameters. Remineralization (R) values are shown for the decrease in ^{234}Th flux calculated between Ez (base of the euphotic zone) and 100 m below it (R_{100}) and from 100 m below the Ez to 200 m below Ez (R_{200}). R values were not reported if no remineralization (^{234}Th excess) feature was observed (Fig. 3), fluxes increased below Ez, or uncertainties were >3 times the R values. Adjusted ^{234}Th fluxes incorporate the upwelling component (Eq. 5) for stations 1 to 7 (Supp. Table 3) and are the values to be used in determining other fluxes (e.g. particulate organic carbon). Stations are labeled as 'St' in all tables.

Zone	St	Lat S	Lon W	Average Ez for All Casts (m)	^{234}Th Flux at Ez (dpm m^{-2} d^{-1})	Upwelling-Adjusted ^{234}Th Flux at Ez (dpm m^{-2} d^{-1})	Upwelling-Adjusted ^{234}Th Flux at Ez + 100 (dpm m^{-2} d^{-1})	Decrease in ^{234}Th, R_{100} (dpm m^{-2} d^{-1})	Decrease in ^{234}Th, R_{200} (dpm m^{-2} d^{-1})
Shelf	2	12.0	77.4	30	1400 ± 30	4000 ± 600			
	3	12.0	77.7	25	1100 ± 40	5000 ± 1000	7000 ± 1000		
	4	12.0	77.8	43	1000 ± 100	4000 ± 900	6000 ± 1000		
	5	12.0	78.2	50	1700 ± 70	4000 ± 700	6000 ± 800		
	1	12.0	79.2	66	2000 ± 90	4000 ± 800	6000 ± 900		
Offshore	6	12.0	81.5	80	1900 ± 100	4000 ± 700	4000 ± 700		
	7	12.0	84.0	94	2000 ± 100	3000 ± 400	2000 ± 400	700 ± 600	500 ± 800
	8	12.0	86.5	105	2300 ± 200	2300 ± 100	2000 ± 200	500 ± 200	300 ± 400
	9	12.0	89.0	109	1400 ± 100	1400 ± 100	200 ± 200	1200 ± 200	200 ± 400
	10	12.0	91.5	121	1600 ± 300	1600 ± 200	1000 ± 300	600 ± 300	400 ± 400
	11	12.0	94.0	130	1900 ± 200	1900 ± 100	1600 ± 200	300 ± 200	
	12	13.0	96.5	124	1400 ± 200	1400 ± 200	1100 ± 200	300 ± 300	500 ± 400
	13	14.0	99.0	139	1200 ± 200	1200 ± 100	800 ± 300	400 ± 300	400 ± 300
	14	15.0	101.5	164	2700 ± 300	2700 ± 200	2400 ± 300	300 ± 300	
	15	16.0	104.0	168	2200 ± 200	2200 ± 100	1500 ± 200	700 ± 300	700 ± 400

Zone	St	Lat	Long	Average Ez for All Casts (m)	^{234}Th Flux at Ez (dpm m^{-2} d^{-1})	Upwelling-Adjusted ^{234}Th Flux at Ez (dpm m^{-2} d^{-1})	Upwelling-Adjusted ^{234}Th Flux at Ez + 100 (dpm m^{-2} d^{-1})	Decrease in ^{234}Th, R_{100} (dpm m^{-2} d^{-1})	Decrease in ^{234}Th, R_{200} (dpm m^{-2} d^{-1})
Gyre	16	-15.4	-106.5	150	2100 ± 300	2100 ± 300	1600 ± 300	500 ± 300	200 ± 400
	17	-15.0	-109.2	163	1300 ± 200	1300 ± 200	700 ± 300	500 ± 300	500 ± 300
	18	-15.0	-112.8	174	1600 ± 200	1600 ± 200	1000 ± 400	600 ± 300	
	20	-15.0	-113.5	191	1600 ± 300	1600 ± 300	1300 ± 400	300 ± 300	
	21	-14.8	-115.0	167	1300 ± 200	1300 ± 200	900 ± 300	400 ± 300	
	22	-14.4	-117.5	179	2000 ± 200	2000 ± 200	1600 ± 400	400 ± 300	900 ± 300
	23	-14.0	-120.0	169	1700 ± 300	1700 ± 300	1400 ± 400	300 ± 300	
	24	-13.3	-122.5	163	1300 ± 300	1300 ± 300	1000 ± 400	300 ± 300	500 ± 300
	25	-12.5	-125.0	163	1400 ± 200	1400 ± 200	1500 ± 500		
	26	-11.7	-128.0	169	1000 ± 200	1000 ± 200	800 ± 500	300 ± 400	
	27	-11.7	-130.0	184	1500 ± 300	1500 ± 300	1500 ± 400		
	28	-11.6	-132.5	162	1500 ± 200	1500 ± 200	900 ± 500	500 ± 400	
	29	-11.6	-135.0	175	1300 ± 200	1300 ± 200	1100 ± 400	200 ± 400	
	30	-11.6	-137.0	168	1400 ± 200	1400 ± 200	1100 ± 400	200 ± 300	700 ± 300
	31	-11.3	-140.0	146	1600 ± 200	1600 ± 200	1600 ± 300		
	32	-11.0	-142.9	153	2000 ± 200	2000 ± 200	1600 ± 300	400 ± 300	400 ± 400
	33	-10.9	-145.0	186	1800 ± 300	1800 ± 300	1800 ± 400		
	34	-10.8	-147.5	175	1600 ± 200	1600 ± 200	1400 ± 400	200 ± 300	
	35	-10.3	-150.0	170	1900 ± 200	1900 ± 200	2100 ± 400		
	36	-10.5	-152.0	179	1200 ± 400	1200 ± 400	800 ± 600	400 ± 400	300 ± 600

Table 2: Summary of zonal characteristics for the Shelf, Offshore, and Gyre zones. Included are ^{234}Th estimates, carbon results, and biologically-relevant parameters. MODIS and SeaWIFS sources for NPP are discussed in Section 2.2.3. Ez-ratios are calculated using ^{234}Th-derived POC export.

	Shelf	**Offshore**	**Gyre**
Longitude range	77° W to 80° W	80° W to 105° W	105° W to 155° W
Average MLD (m)	21 ± 16	59 ± 19	60 ± 11
Average Ez (m)	43 ± 16	123 ± 28	169 ± 12
Depth of oxygen minimum (m)	90 ± 45	200 ± 85	337 ± 25
Oxygen Saturation % at minimum	0.4 ± 0.1	1.5 ± 2	14 ± 8
Upper ODZ boundary (m)	54 ± 12	152 ± 56	
Subsurface LSF C:Th (Ez to 400 m)	1.4 ± 0.3	0.9 ± 0.2	0.7 ± 0.1
Subsurface SSF C:Th (Ez to 400 m)	1.2 ± 0.5	0.6 ± 0.3	0.5 ± 0.2
Subsurface LSF N:Th (Ez to 400 m)	0.2 ± 0.05	0.10 ± 0.04	0.08 ± 0.03
Subsurface SSF N:Th (Ez to 400 m)	0.2 ± 0.09	0.07 ± 0.06	0.07 ± 0.05
^{234}Th flux at Ez (dpm m^{-2} d^{-1})	1400 ± 400	1900 ± 500	1600 ± 300
^{234}Th flux at 100 m (dpm m^{-2} d^{-1})	1600 ± 400	1800 ± 300	1100 ± 200
Adjusted ^{234}Th flux at Ez (dpm m^{-2} d^{-1})	4200 ± 400	2400 ± 1000	1600 ± 300
Decrease in ^{234}Th from Ez to 100 m below: R_{100} (dpm m^{-2} d^{-1})		600 ± 300	400 ± 100
Decrease in ^{234}Th from Ez+100 to Ez+200: R_{200} (dpm m^{-2} d^{-1})		400 ± 200	500 ± 200
POC flux at Ez (mmolC m^{-2} d^{-1})	42 ± 27	3 ± 2	1.1 ± 0.2
POC flux at 100 (mmolC m^{-2} d^{-1})	9 ± 1	3 ± 2	1.9 ± 0.4
PON flux at Ez (mmolN m^{-2} d^{-1})	6 ± 4	0.4 ± 0.3	0.1 ± 0.03
GBC14 modeled POC export (mmolC m^{-2} d^{-1})	20 ± 5	6 2	5 1
MODIS-based 16-day NPP (mmolC m^{-2} d^{-1})	114 ± 52	50 ± 7	47 ± 6
SeaWIFS-based 8-day NPP (mmolC m^{-2} d^{-1})	99 ± 21	53 ± 4	54 ± 4
SeaWIFS-based annual NPP (mmolC m^{-2} d^{-1})	96 ± 19	52 ± 5	56 ± 5
Ez-ratio (POC flux at Ez/MODIS NPP)	0.3 ± 0.2	0.06 ± 0.04	0.02 ± 0.005
Carbon T_{100} (flux at 100 m below Ez/export at Ez)	0.4 0.4	0.6 ± 0.2	0.8 ± 0.1
Carbon T_{200} (flux at 200 m below Ez/export at Ez)	0.5 0.5	0.4 ± 0.2	0.4 ± 0.2
Average % of POC exported at 100 m below Ez (Ez-ratio x T_{100})	10 3	3 ± 2	2 ± 0.3

Table 3: ^{234}Th-derived carbon and nitrogen export and remineralization results, net primary production, and Ez-ratios by station. MODIS and SeaWIFS sources for NPP are discussed in Section 2.2.3. All carbon fluxes, nitrogen fluxes, and NPP are reported in mmol m^{-2} d^{-1}. Ez-ratios were calculated using ^{234}Th-derived POC export and represent the export of carbon at Ez divided by NPP. T_{100} values represent the POC flux at 100 m below the Ez divided by the POC flux at Ez. The GBC14 modeled export comes from the global model used in Siegel et al. (2014). The percent of POC exported at 100 m below Ez is equivalent to the Ez-ratio multiplied by the T_{100} value.

St	Derived C:Th at Ez (µmol dpm^{-1})	Derived N:Th at Ez (µmol dpm^{-1})	POC flux at Ez	PON flux at Ez	GBC14 model POC flux at Ez	16-day MODIS-based NPP	8-day SeaWIFS-based NPP	Annual SeaWIFS-based NPP	Ez-ratio	T_{100}	T_{200}	%POC export at 100 m below Ez
2	13 ± 4	2.2 ± 0.6	50 ± 20	9 ± 3	24	188	112	115	0.3			
3	15 ± 4	2.4 ± 0.6	80 ± 30	12 ± 4	24	147	112	115	0.5	0.1		7
4	9 ± 4	1.5 ± 0.6	40 ± 17	6 ± 3	24	93	113	115	0.4	0.2	0.2	9
5	7 ± 4	1.1 ± 0.6	30 ± 20	4 ± 2	16	80	81	72	0.4	0.3	0.2	11
1	2 ± 4	0.2 ± 0.1	8 ± 17	0.7 ± 0.2	14	63	77	63	0.1	1	1	13
6	2.0 ± 0.6	0.3 ± 0.1	9 ± 3	1.2 ± 0.5	9	61	60	56	0.1	0.4	0.4	7
7	2 ± 1	0.2 ± 0.1	5 ± 2	0.7 ± 0.3	8	51	57	54	0.1	0.4	0.3	4
8	1 ± 1	0.2 ± 0.1	3 ± 1	0.4 ± 0.2	6	53	54	54	0.06	0.5	0.4	3
9	1 ± 1	0.2 ± 0.1	2.0 ± 0.8	0.3 ± 0.1	6	53	54	53	0.04	0.1	0.0	0.4
10	1.1 ± 0.6	0.1 ± 0.1	2.0 ± 0.9	0.2 ± 0.2	5	56	54	52	0.04	0.5	0.3	2
11	0.9 ± 0.2	0.1 ± 0.1	2.0 ± 0.5	0.2 ± 0.2	5	49	52	51	0.04	0.9		3
12	1.0 ± 0.6	0.1 ± 0.1	1.4 ± 0.8	0.2 ± 0.1	5	46	50	52	0.03	0.7	0.4	2
13	0.9 ± 0.2	0.1 ± 0.04	1.1 ± 0.3	0.1 ± 0.05	4	52	48	50	0.02	0.7	0.4	1
14	0.9 ± 0.2	0.1 ± 0.04	3 ± 1	0.3 ± 0.1	4	43	46	47	0.07	0.9	0.8	6
15	0.9 ± 0.2	0.1 ± 0.04	2.1 ± 0.5	0.2 ± 0.1	4	36	45	44	0.06	0.7	0.4	4

St	Derived C:Th at Ez (µmol dpm^{-1})	Derived N:Th at Ez (µmol dpm^{-1})	POC flux at Ez	PON flux at Ez	GBC14 model POC flux at Ez	16-day MODIS-based NPP	8-day SeaWIFS-based NPP	Annual SeaWIFS-based NPP	Ez-ratio	T_{100}	T_{200}	%POC export at 100 m below Ez
16	0.7 ± 0.1	0.08 ± 0.03	1.0 ± 0.2	0.2 ± 0.1	4	44	48	48	0.02	0.8	0.7	2
17	0.7 ± 0.1	0.08 ± 0.03	1.0 ± 0.2	0.11 ± 0.03	4	42	50	49	0.02	0.6	0.2	1
18	0.7 ± 0.1	0.08 ± 0.03	1.0 ± 0.2	0.13 ± 0.04	5	51	53	50	0.02	0.6		1
20	0.7 ± 0.1	0.08 ± 0.03	1.0 ± 0.2	0.13 ± 0.04	5	46	53	50	0.02	0.8		2
21	0.7 ± 0.1	0.08 ± 0.03	0.9 ± 0.2	0.10 ± 0.03	5	46	54	52	0.02	0.7		1
22	0.7 ± 0.1	0.08 ± 0.03	1.4 ± 0.2	0.17 ± 0.05	4	52	51	52	0.03	0.8	0.3	2
23	0.7 ± 0.1	0.08 ± 0.03	1.2 ± 0.2	0.14 ± 0.05	5	58	52	52	0.02	0.8		2
24	0.7 ± 0.1	0.08 ± 0.03	0.9 ± 0.2	0.10 ± 0.04	5	46	56	53	0.02	0.8	0.4	2
25	0.7 ± 0.1	0.08 ± 0.03	1.0 ± 0.2	0.12 ± 0.04	5	48	58	55	0.02			
26	0.7 ± 0.1	0.08 ± 0.03	0.7 ± 0.2	0.09 ± 0.03	6	42	60	57	0.02	0.7		1
27	0.7 ± 0.1	0.08 ± 0.03	1.1 ± 0.2	0.12 ± 0.04	5	47	59	56	0.02			
28	0.7 ± 0.1	0.08 ± 0.03	1.0 ± 0.2	0.12 ± 0.04	6	47	59	56	0.02	0.7		1
29	0.7 ± 0.1	0.08 ± 0.03	0.9 ± 0.2	0.10 ± 0.04	6	55	60	56	0.02	0.8		1
30	0.7 ± 0.1	0.08 ± 0.03	1.0 ± 0.2	0.11 ± 0.04	7	51	63	58	0.02	0.8	0.3	2
31	0.7 ± 0.1	0.08 ± 0.03	1.1 ± 0.2	0.13 ± 0.04	8	46	67	62	0.02			
32	0.7 ± 0.1	0.08 ± 0.03	1.4 ± 0.2	0.16 ± 0.05	6	54	58	57	0.03	0.8	0.6	2
33	0.7 ± 0.1	0.08 ± 0.03	1.2 ± 0.2	0.14 ± 0.05	7	44	60	58	0.03			
34	0.7 ± 0.1	0.08 ± 0.03	1.2 ± 0.2	0.13 ± 0.04	6	45	56	55	0.03	0.9		2
35	0.7 ± 0.1	0.08 ± 0.03	1.4 ± 0.2	0.16 ± 0.05	5	36	53	53	0.04			
36	0.7 ± 0.1	0.08 ± 0.03	0.8 ± 0.2	0.10 ± 0.03	5	34	52	52	0.02	0.7	0.4	2

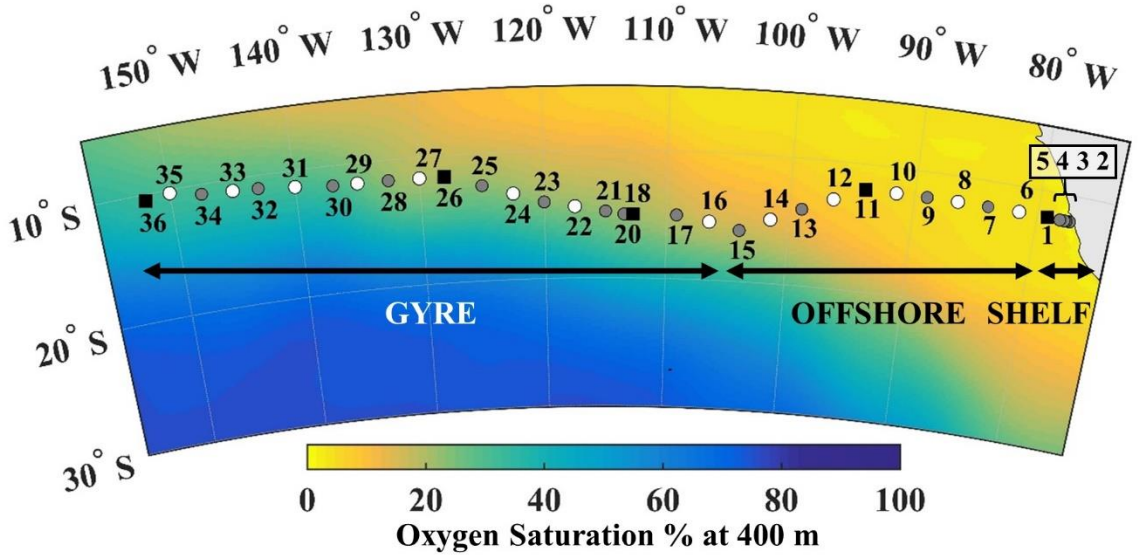

Figure 1: Station locations with oxygen saturation at 400 m. Zonal designations are shown for stations 1-5 (Shelf), 6-15 (Offshore), and 16-36 (Gyre). Oxygen data are a historical compilation (NOAA World Ocean Atlas, 2009). Total and particulate ^{234}Th samples were taken at a minimum of 24 discrete depths throughout the full water column at super stations (black squares) and 8 to 16 depths at coastal and full stations (grey circles). Only total ^{234}Th was measured in the upper 1000 m at demi stations (12 depths; white circles).

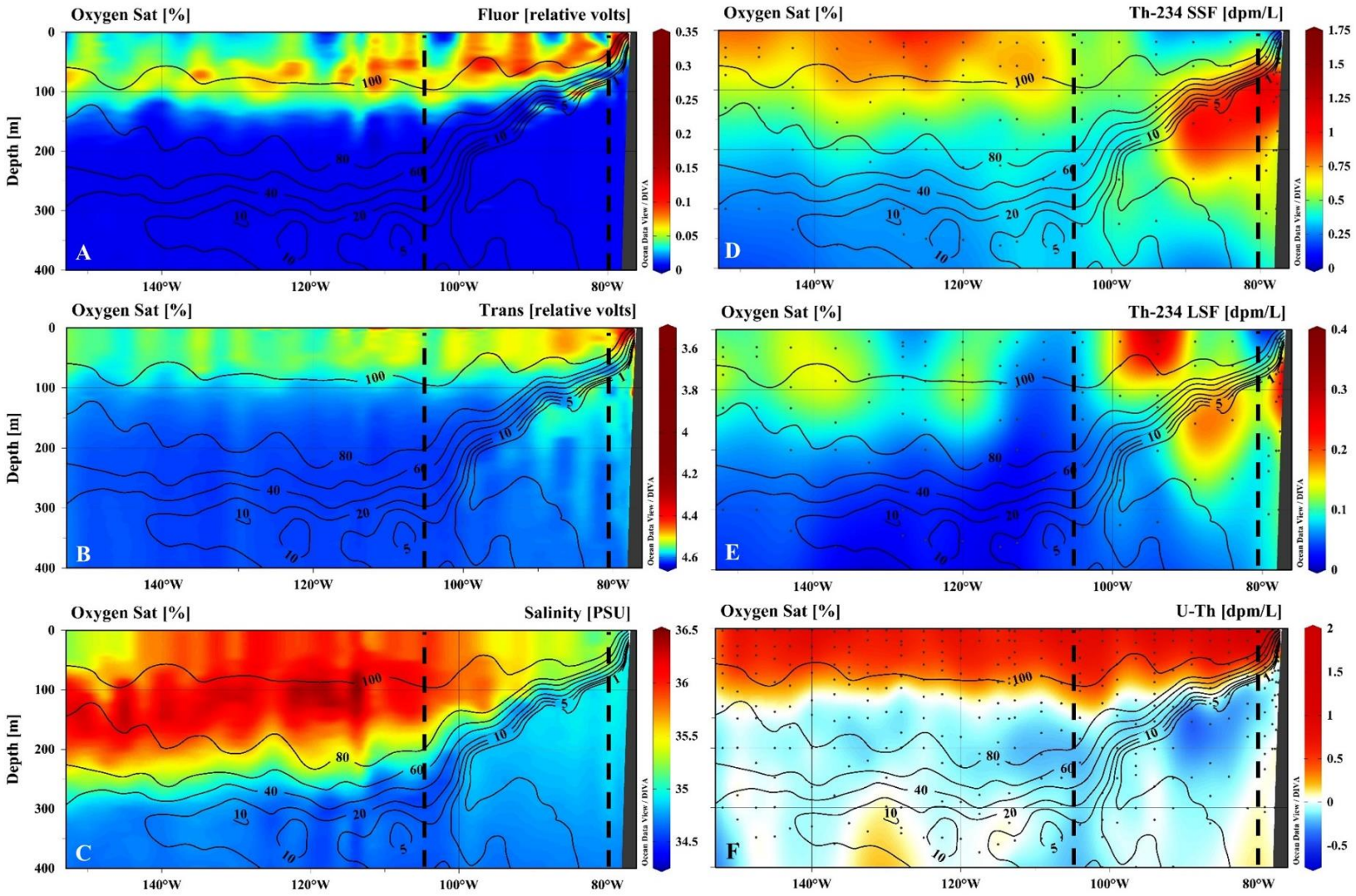

Figure 2: ^{234}Th results and relevant CTD sensor parameters with oxygen saturation %. Oxygen saturation (contours) is shown relative to Fluorescence (A), Light Transmission (B), Salinity (C), small particle ^{234}Th activities (1−51 µm, D), large particle ^{234}Th activities (>51 µm, E) and ^{238}U–^{234}Th activities (F). Zones corresponding to Fig. 1 are delineated by dashed lines. Transmission, Salinity, and Fluorescence were from the ODF rosette. Oxygen saturation contours were determined using only data from the total ^{234}Th cast.

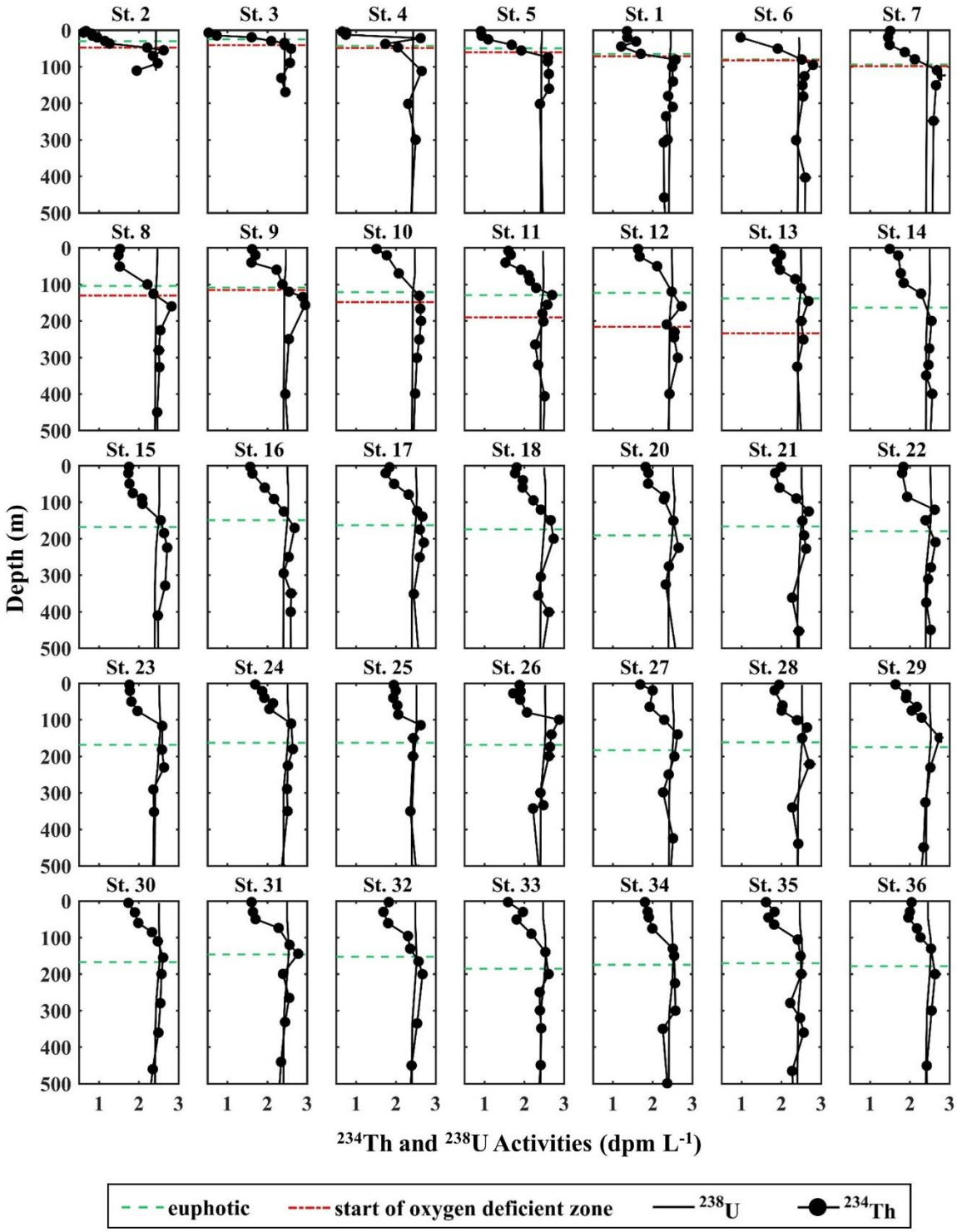

Figure 3: ^{234}Th and ^{238}U activity profiles in dpm L^{-1} for the upper 500 m of the water column. The average Ez for all casts is shown for each station (green) with the start of the oxygen deficient zone (red) for those stations with ODZs. All presented data was used in the export and remineralization flux calculations.

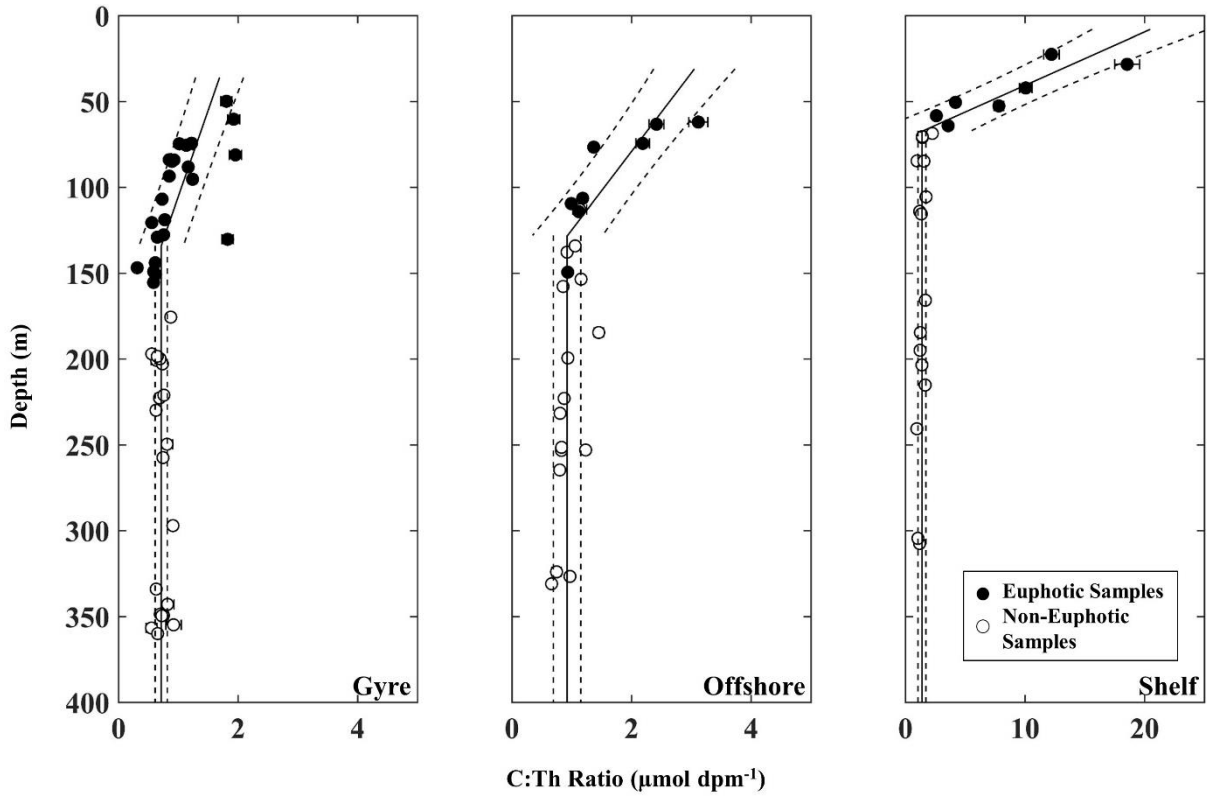

Figure 4: Carbon:^{234}Th on large particles (>51 µm) in µmol dpm^{-1} for the upper 400 m. Best fit linear regressions are shown for euphotic samples along with the average ratio for samples collected below the base of the euphotic to 400 m (solid lines). Both are shown with 1 standard deviation (dotted lines). Mixed layer samples are not shown and not included in ratio calculations.

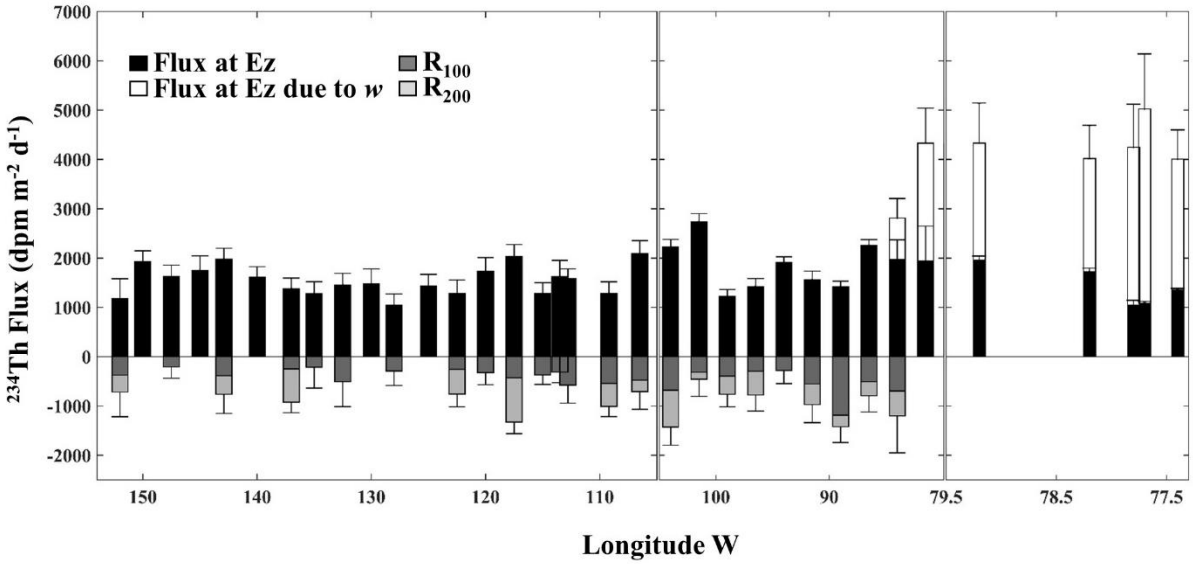

Figure 5: ^{234}Th Export at Ez and remineralization through the 200 m below Ez. Calculated ^{234}Th export is shown as the ^{234}Th flux without upwelling (black) and additional flux due to upwelling *w* (white) at the base of the euphotic zone (Ez). The decrease in flux through the first 100 m below Ez (R_{100}; dark grey) and subsequent 100 m to 200 m below Ez (R_{200}; light grey) are also shown. Values of R_{100} and R_{200} are negative because ^{234}Th flux decreases below Ez at the stations indicated. See Table 1 for additional details on R values.

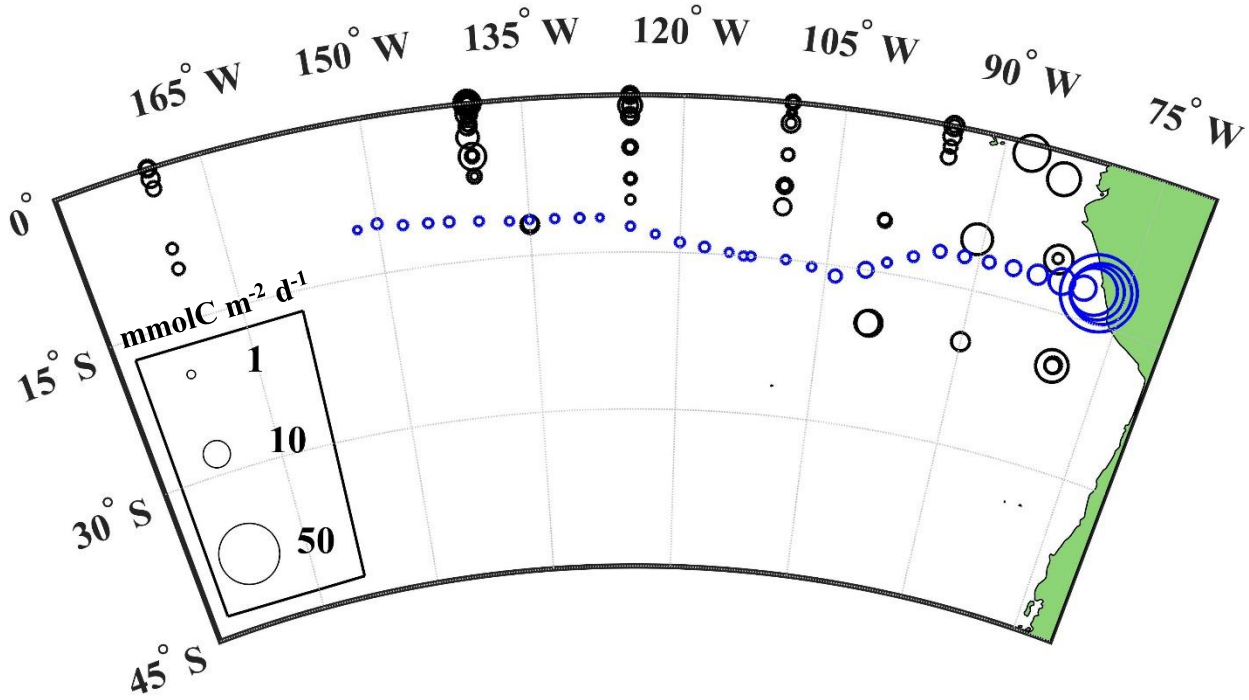

Figure 6: Regional ^{234}Th-derived carbon fluxes. The magnitude of POC flux is indicated by circle area at each location. All prior carbon export values for this region are shown (black). Export was calculated at depths ranging from 100 m to 200 m and in different seasons. The equatorial data is from various studies compiled by Le Moigne et al. (2013) and the remaining locations were from Haskell et al. (2013). POC fluxes from this GEOTRACES campaign, calculated at Ez, are shown in blue (Table 3).

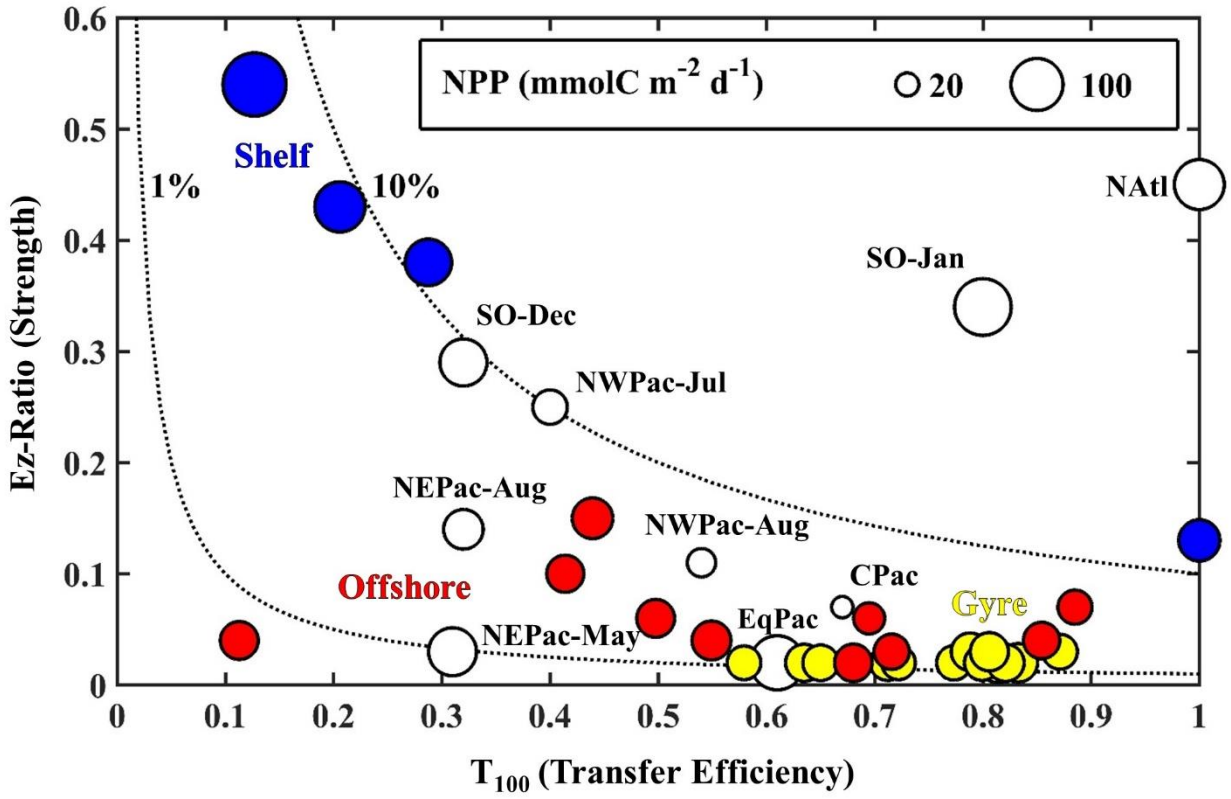

Figure 7: ^{234}Th-derived Ez-ratios (export at Ez/NPP) and T_{100} (flux at 100 m below Ez/export at Ez) values for POC. Station specific values from this campaign are shown with results from Buesseler and Boyd (2009). The prior regions of study include the following: NAtl (NABE, North Atlantic Bloom Experiment; 47° N, 20° W), NWPac (K2, Northwest Pacific; 47° N, 160° E), CPac (ALOHA, Central North Pacific; 22° N, 158° W), EqPac (Equatorial Pacific; 0° N, 140° W), SO (KIWI, Southern Ocean; 61.5° S to 65.5° S, 170° W), and NEPac (Station Papa, Northeast Pacific; 50° N, 145° W). The area of the circles represents NPP in mmolC m^{-2} d^{-1}. The 1% and 10% contour lines show the relationships between the POC flux 100 m below Ez and NPP.

Supplemental Table 1: Depth of relevant physical parameters for the shallow ^{234}Th cast (Cast) and the average of all ODF and GEOTRACES rosette casts. Average mixed layer and Ez values (Ohnemus et al., 2016) were used for flux and upwelling calculations to allow comparison between this study and others. The shallow ^{234}Th cast depths are shown here for reference. As described in the text and shown in Supp. Figs. 1 and 2, oxygen data was highly variable cast to cast. Only the ^{234}Th shallow cast (ODF rosette) values are shown here and used in this study, although values for the GEOTRACES rosette are described in Ohnemus et al. (2016).

Zone	St	Average MLD for all casts (m)	Cast MLD (m)	Average Ez for all casts (m)	Cast Ez depth (m)	Cast oxygen minimum depth (m)	Cast oxygen saturation % at minimum	Cast upper ODZ boundary (m)
Shelf	2	8	10	30	28	69	0.4	48
	3	8	12	25	22	--	0.5	41
	4	16	18	43	46	63	0.3	49
	5	25	28	50	47	72	0.4	61
	1	46	52	66	59	79	0.3	72
Offshore	6	31	31	80	76	116	0.3	83
	7	50	59	94	128	103	0.4	99
	8	46	51	105	111	149	0.5	131
	9	53	51	109	101	133	0.2	116
	10	78	80	121	113	161	0.3	148
	11	51	56	130	137	198	0.3	190
	12	41	41	124	127	228	0.5	216
	13	78	67	139	126	249	0.6	234
	14	89	91	164	158	304	5	--
	15	74	74	168	162	362	7	--

Zone	St	Average MLD for all casts (m)	Cast MLD (m)	Average Ez for all casts (m)	Cast Ez depth (m)	Cast oxygen minimum depth (m)	Cast oxygen saturation % at minimum	Cast upper ODZ boundary (m)
Gyre	16	56	56	150	140	350	5	--
	17	57	49	163	145	333	5	--
	18	36	31	174	165	358	5	--
	20	49	60	191	168	380	13	--
	21	59	63	167	142	357	4	--
	22	56	54	179	162	373	13	--
	23	45	51	169	164	375	11	--
	24	54	57	163	153	344	4	--
	25	76	76	163	156	353	12	--
	26	57	65	169	167	324	7	--
	27	60	58	184	171	302	10	--
	28	67	71	162	168	332	11	--
	29	66	67	175	154	325	16	--
	30	74	76	168	172	338	16	--
	31	65	61	146	126	332	9	--
	32	84	78	153	142	313	22	--
	33	65	64	186	176	325	26	--
	34	58	58	175	174	284	29	--
	35	67	70	170	169	306	27	--
	36	60	60	179	163	341	28	--

Supplemental Table 2: Results for 100 m calculations. For comparison with flux calculations at the base of the euphotic zone, fluxes for ^{234}Th (original and upwelling-adjusted) and particulate organic carbon are included.

Zone	St	^{234}Th flux at 100 m (dpm m^{-2} d^{-1})	Upwelling-adjusted ^{234}Th flux at 100 m (dpm m^{-2} d^{-1})	POC flux at 100 m (mmol m^{-2} d^{-1})
Shelf	2	1800 ± 100	7000 ± 1000	10 ± 3
	3	900 ± 100	7000 ± 2000	10 ± 3
	4	1300 ± 200	6000 ± 1000	8 ± 2
	5	1800 ± 100	6000 ± 1000	8 ± 2
	1	2000 ± 100	6000 ± 1000	8 ± 2
Offshore	6	1800 ± 200	4000 ± 1000	7 ± 3
	7	1900 ± 100	3000 ± 1000	4 ± 2
	8	2200 ± 200	2200 ± 200	3 ± 1
	9	1400 ± 100	1400 ± 100	2 ± 1
	10	1700 ± 200	1700 ± 200	3 ± 1
	11	1900 ± 100	1900 ± 100	3 ± 1
	12	1400 ± 200	1400 ± 200	2 ± 1
	13	1300 ± 200	1300 ± 200	2 ± 1
	14	2200 ± 200	2200 ± 200	3 ± 1
	15	2000 ± 100	2000 ± 100	3 ± 1
Gyre	16	1900 ± 200	1900 ± 200	2 ± 0.7
	17	1400 ± 100	1400 ± 100	2 ± 0.5
	18	1600 ± 100	1600 ± 100	2 ± 0.6
	20	1500 ± 200	1500 ± 200	2 ± 0.5
	21	1400 ± 200	1400 ± 200	1 ± 0.5
	22	1900 ± 200	1900 ± 200	2 ± 0.7
	23	1800 ± 200	1800 ± 200	2 ± 0.7
	24	1400 ± 200	1400 ± 200	2 ± 0.5
	25	1500 ± 100	1500 ± 100	2 ± 0.5
	26	1400 ± 200	1400 ± 200	2 ± 0.5
	27	1500 ± 200	1500 ± 200	2 ± 0.6
	28	1500 ± 200	1500 ± 200	2 ± 0.6
	29	1500 ± 200	1500 ± 200	2 ± 0.5
	30	1400 ± 200	1400 ± 200	1 ± 0.5
	31	1700 ± 200	1700 ± 200	2 ± 0.6
	32	1800 ± 200	1800 ± 200	2 ± 0.7
	33	1600 ± 200	1600 ± 200	2 ± 0.6
	34	1600 ± 100	1600 ± 100	2 ± 0.6
	35	1800 ± 200	1800 ± 200	2 ± 0.7
	36	1100 ± 100	1100 ± 100	1 ± 0.4

Supplemental Table 3: Parameters used to derive the ^{234}Th flux component due to upwelling in the coastal region. The depth ranges with gradients in ^{234}Th and potential density are shown here with the approximate depth of equilibrium (where the activity of total ^{234}Th first transitions from being lower than the activity of ^{238}U to higher than the local ^{238}U activity). The depth of equilibrium was approximated at each station using the slope of the ^{234}Th gradient from the surrounding sampling points. The depth boundaries where the gradients existed in both ^{234}Th and potential density generally coincided, but some variability was observed due to the lower sampling resolution of ^{234}Th (n = 3 to 8, Fig. 3) compared to that of potential density (n >50, Supp. Fig. 6). To determine the upwelling component of ^{234}Th flux, ^{234}Th gradients from each station were multiplied by ^{7}Be-derived upwelling rates that were calculated directly for stations 1 and 7 (constant upwelling model with 0 m s^{-1} horizontal advection; Kadko 2017), shown in bold and italics, or extrapolated from surrounding stations as indicated (Supp. Fig. 7). A range of models, *w*, and *u* were tested to determine the uncertainty on the upwelling component of ^{234}Th flux (Supp. Fig. 7).

Zone	St	^{234}Th surface gradient depth range (m)	Estimated equilibrium depth (m)	MLD to potential density gradient boundary (m)	^{234}Th gradient with depth (dpm L^{-1} m^{-1})	Range of *w* used to assess model variability (m d^{-1})	Upwelling rate from constant upwelling model (m d^{-1})	Upwelling component of ^{234}Th flux at Ez using constant model (dpm m^{-2} d^{-1})
Shelf	2	6 - 55	57	8 - 56	3.85E-02	2.4 - 4.9	3.0	3000 ± 1000
	3	7 - 35	35	8 - 54	7.14E-02	2.4 - 4.9	3.0	4000 ± 2000
	4	13 - 47	57	16 - 49	3.79E-02	2.4 - 4.9	3.0	3000 ± 1000
	5	25 - 74	69	25 - 67	2.93E-02	2.4 - 4.9	3.0	2000 ± 1000
	1	45 - 81	80	46 - 79	3.74E-02	***2.4*** - ***4.9***	***3.0***	2000 ± 1000
Offshore	6	20 - 80	75	31 - 95	2.55E-02	1.4 - 3.5	2.1	3000 ± 700
	7	40 - 110	96	50 - 101	1.68E-02	***0.4*** - ***2.0***	***1.1***	800 ± 300

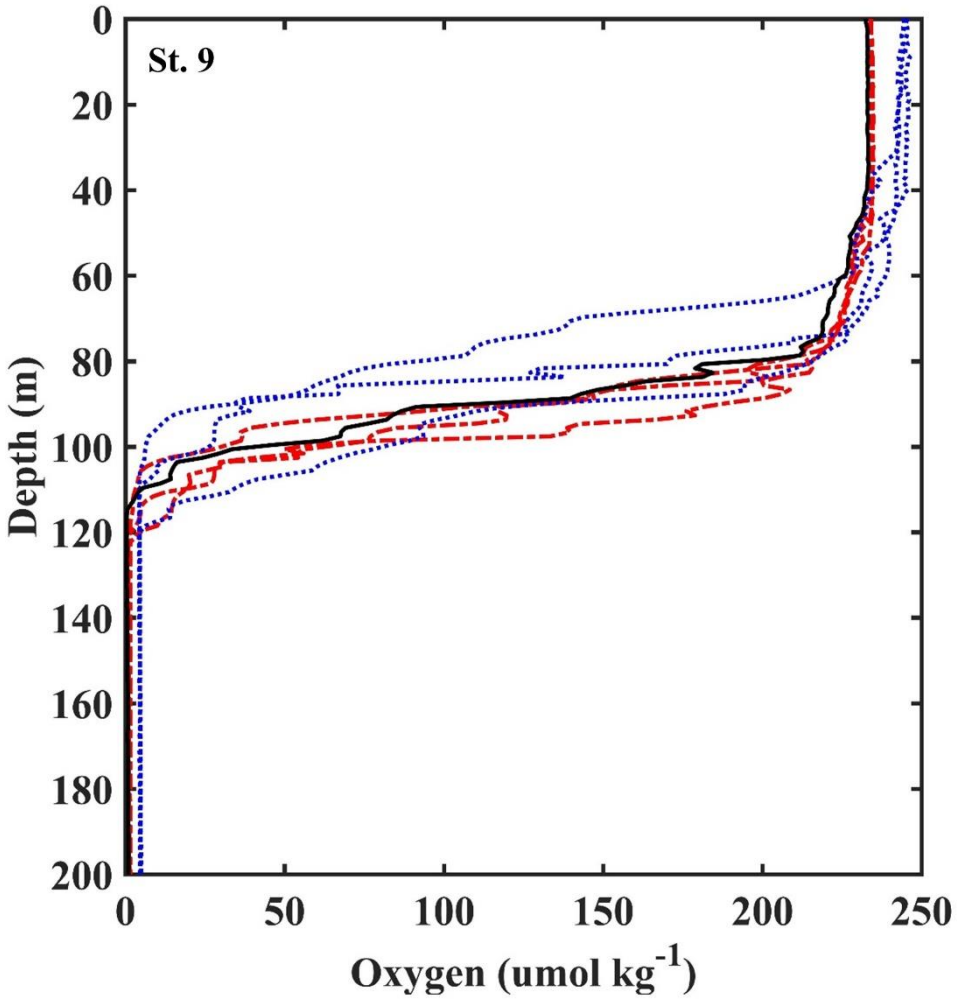

Supplemental Figure 1: Example of inter-cast variability in oxygen. Upcast data taken from station 9 is shown for casts performed with the GEOTRACES rosette CTD (red dashed) and the Ocean Data Facility rosette CTD (blue dashed). The data from the 3rd cast of the 7 shown here was the cast where ^{234}Th was sampled (solid black line).

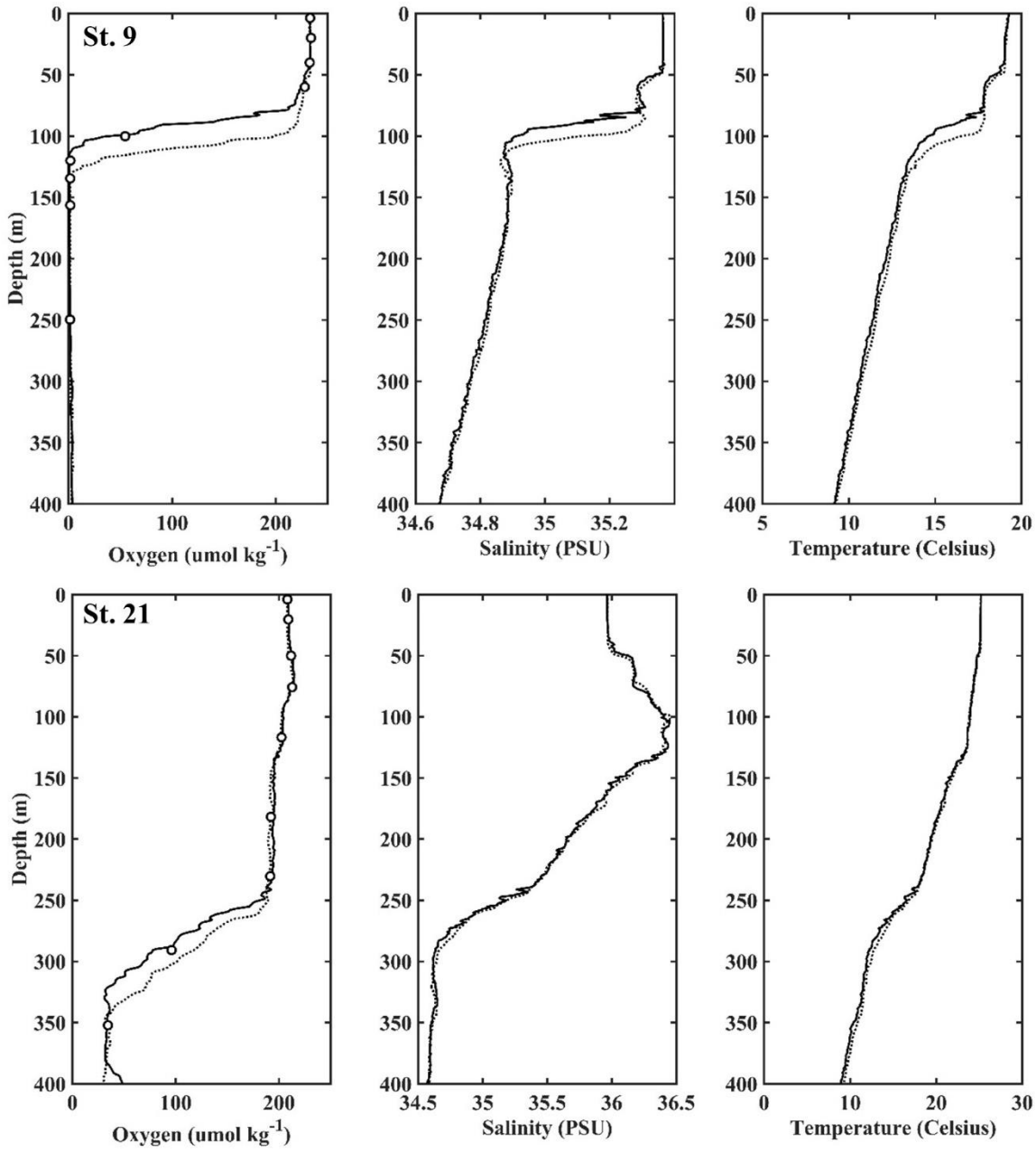

Supplemental Figure 2: Examples of intra-cast variability in oxygen for casts where ^{234}Th was collected. Downcast data (dashed line) and upcast data (solid line) are shown with bottle-derived oxygen concentrations (circles). Bottle data match the upcast trace because niskins were tripped on the upcast. Substantial oxygen differences occurred between the up and down casts even when no difference was observed in salinity or temperature. This data suggests that only upcast traces should be used to estimate in-situ oxygen saturation.

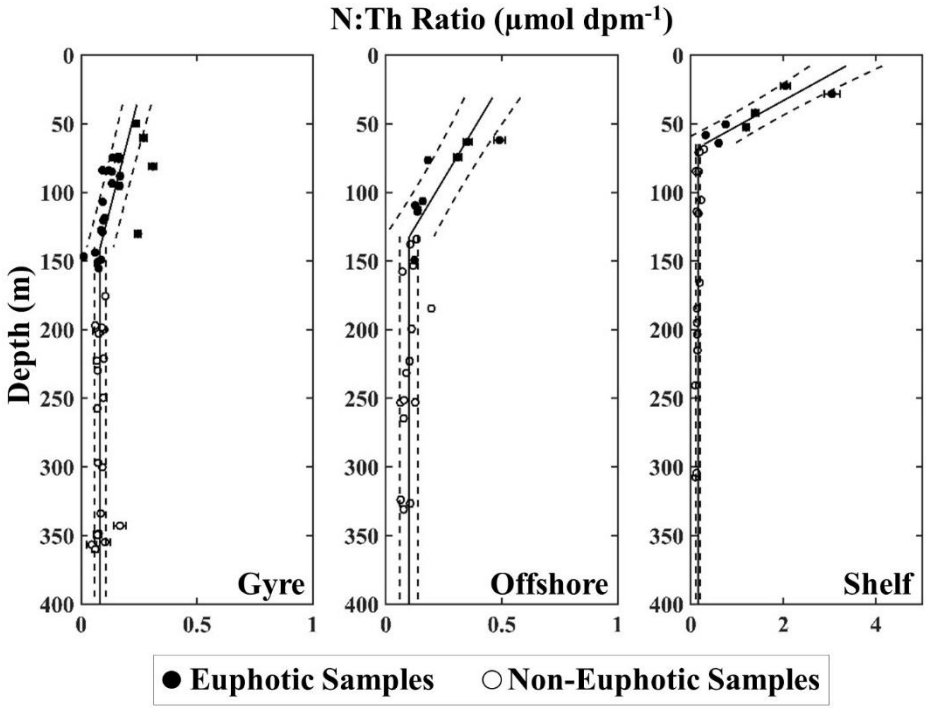

Supplemental Figure 3: Nitrogen:^{234}Th on large particles (>51 µm) in µmol dpm^{-1} for the upper 400 m. Best fit linear regressions are shown for euphotic samples along with the average ratio for samples collected below the base of the euphotic to 400 m (solid lines). Both are shown with 1 standard deviation (dotted lines). Mixed layer samples are not shown and not included in ratio calculations.

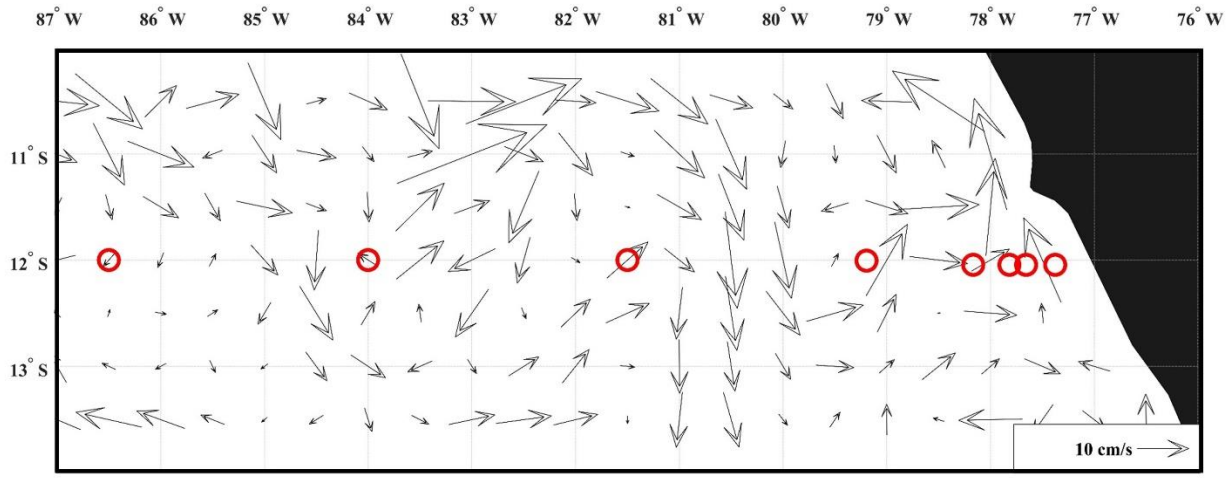

Supplemental Figure 4: Average surface current velocities for October 2013. Geostrophic current velocities were obtained from NOAA for the month prior to the sampling of coastal stations (October; http://pifsc-oceanwatch.irc.noaa.gov/thredds/catalog.html). Stations 1 to 8 are shown where red circles indicate location and approximate size of a 5 cm s^{-1} current (diameter of circle).

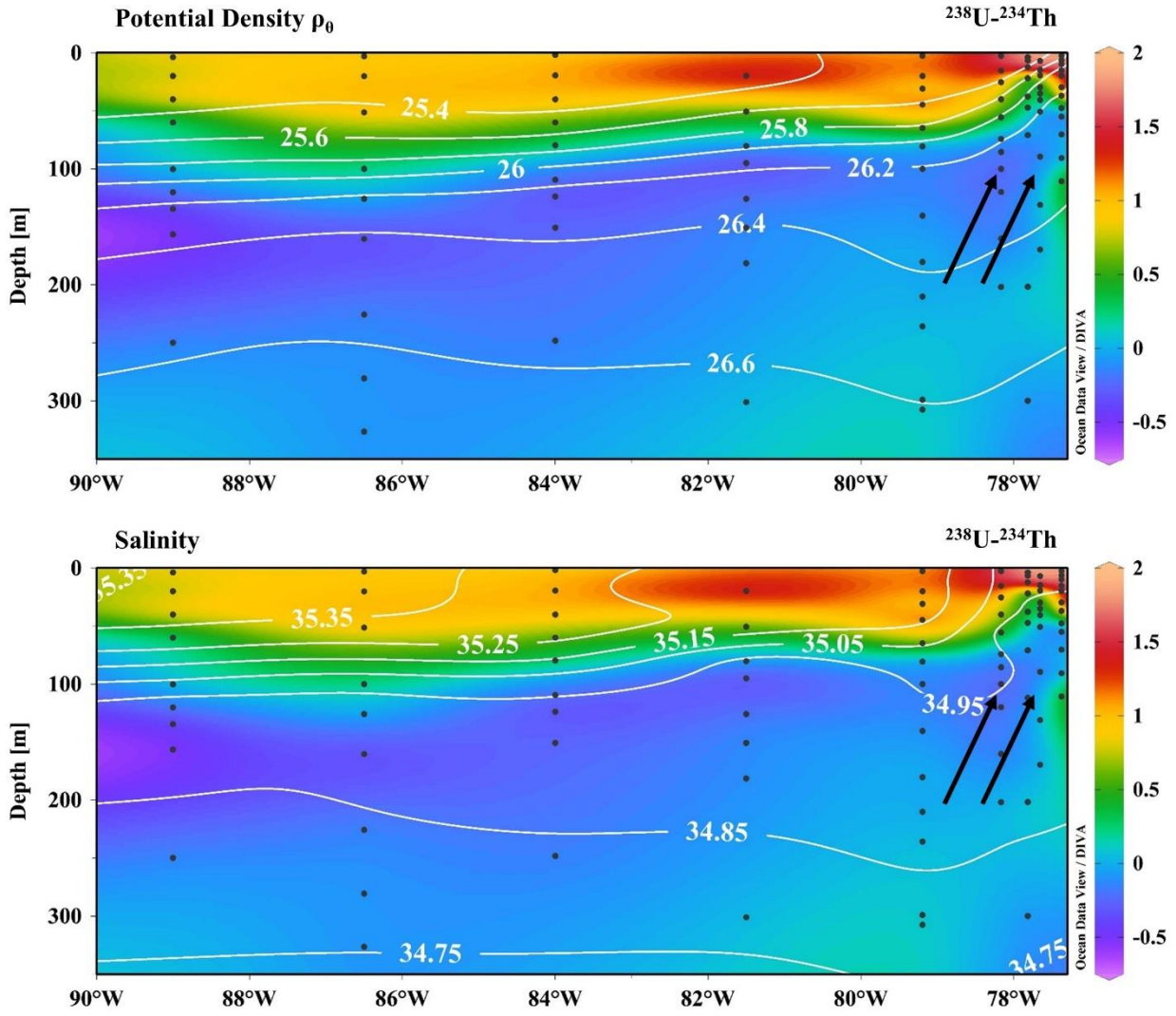

Supplemental Figure 5: ^{238}U minus ^{234}Th activity (colors) with density anomaly (ρ_0) and salinity contours. Arrows show the proposed direction of upwelling, which would bring deeper waters close to equilibrium (^{238}U – ^{234}Th ~ 0) to the shelf. The most impacted locations appear to be from 77° W to 78.5° W.

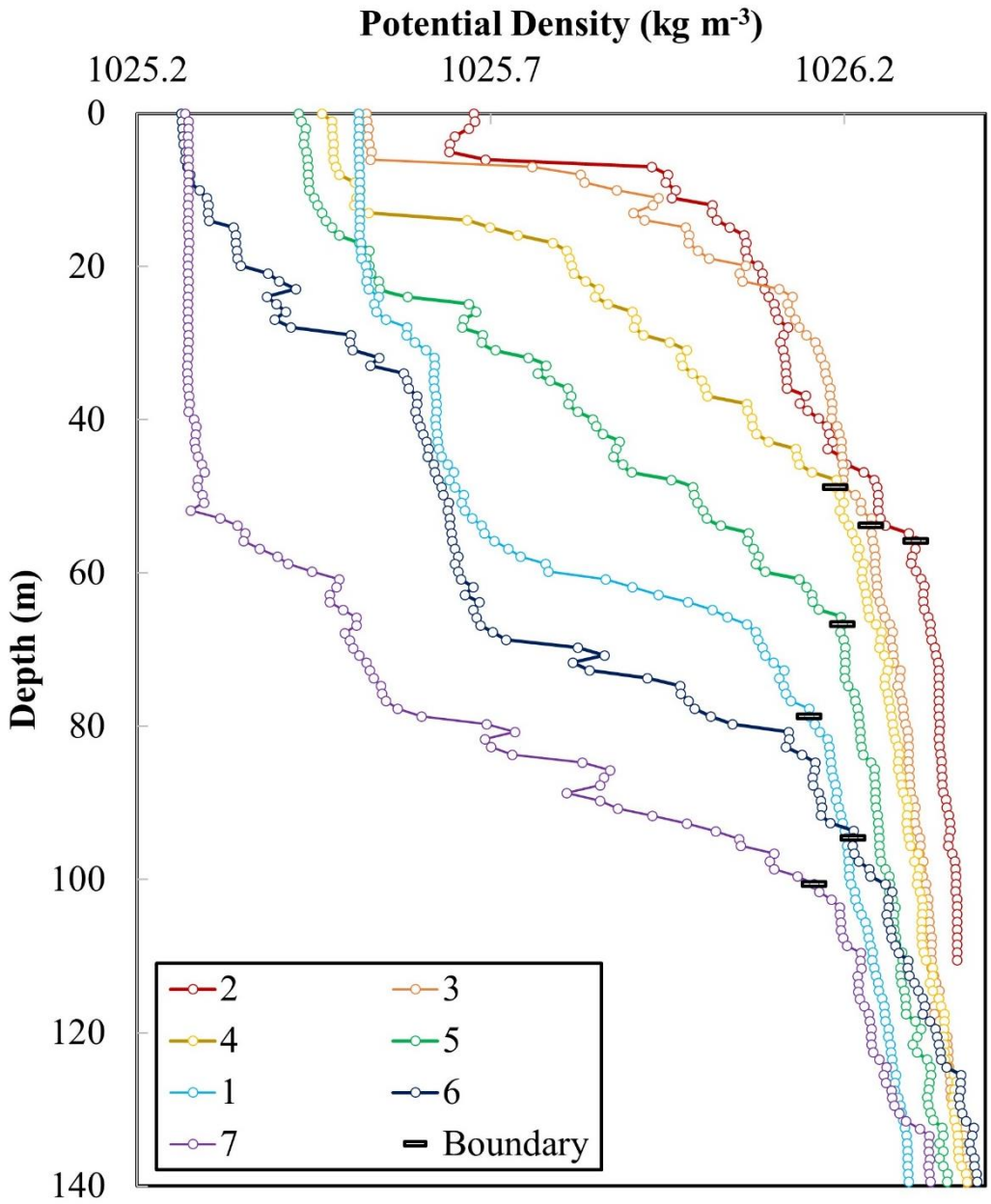

Supplemental Figure 6: Potential density profiles for coastal stations (upper 140 m). Potential density profiles are shown here for Stations 1 through 7 (77º W to 84º W) with a black marker indicating the depth at which successive 1 m data bins showed a difference <0.025 kg m^{-3}. This profile stability (difference <0.025) lasted for at least 40 m below the marker. Due to low variability throughout the entire density profile at station 9, a more stringent difference limit between 1 m bins (0.01) was applied at this station. The marker depth is referred to in the text as the 'Gradient Boundary' (Supp. Table 3) and the depth often coincided with the gradient termination depth for total ^{234}Th. Stations 1 to 7 are shown here because relatively large surface gradients in ^{234}Th with depth were observed in the upper 140 m when compared to profiles from all other stations (85º W to 152º W). Both the density and total ^{234}Th data suggested that upwelling corrections would be most appropriate from the mixed layer to the approximate depth of the marker shown here, where the large gradients cease.

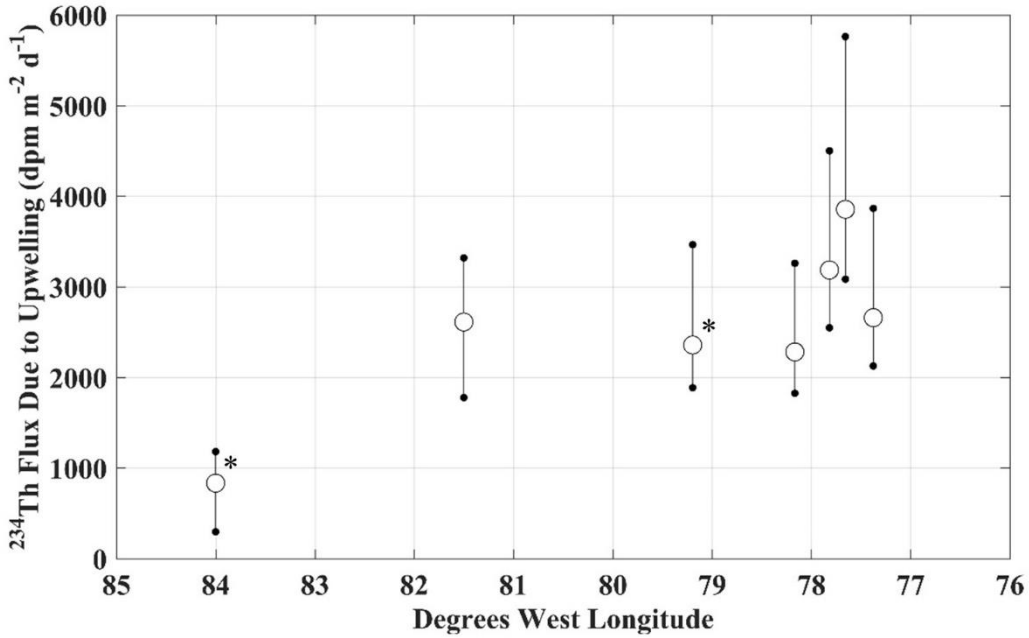

Supplemental Figure 7: Flux of ^{234}Th due to upwelling calculated at the base of the euphotic zone. The stations between 77º W to 84º W (1 to 7) showed large surface gradients in ^{234}Th with depth when compared to the profiles of all other stations. For these 7 stations, the upwelling component of the ^{234}Th flux from Eq. 5, which includes a surface gradient (∂^{234}Th/∂z) and upwelling rate (*w*), is shown here as calculated at Ez. Individual surface gradients were calculated for each station and multiplied by an upwelling rate derived from a constant upwelling model (Kadko, 2017) and these results are shown as open circles. The upwelling component of ^{234}Th flux was set to be non-zero in Eq. 5 at depths between the base of the mixed layer and the density gradient boundary (Supp. Table 3, Supp. Fig. 6). For these stations, Ez was shallower than the gradient boundary. Upwelling rates from Kadko (2017) were only determined for stations 1 (79.2º W at 3 m d^{-1}) and 7 (84º W at 1.1 m d^{-1}), which are indicated by asterisks. The upwelling rate at station 1 was applied to the stations east of 79º W and the rate at 81.5º W was an average of the surrounding stations (2.1 m d^{-1}). Vertical lines about the points represent the potential variability in derived fluxes due to the model used (constant upwelling with depth versus depth-dependent upwelling), *w*, and *u* (horizontal advection). The variability shown incorporated a change in horizontal advection from 0 m s^{-1} to 0.2 m s^{-1}, a change in upwelling from 2.4 m d^{-1} to 4.9 m d^{-1} for station 1 and 0.4 m d^{-1} to 2.0 m d^{-1} for station 7, and the model was changed from constant to depth-dependent (Supp. Table 3). The maximum difference observed at each station between the open circles (0 m s^{-1} horizontal advection, constant model) and the outlier cases (endpoints) was used as the uncertainty on the upwelling flux components.

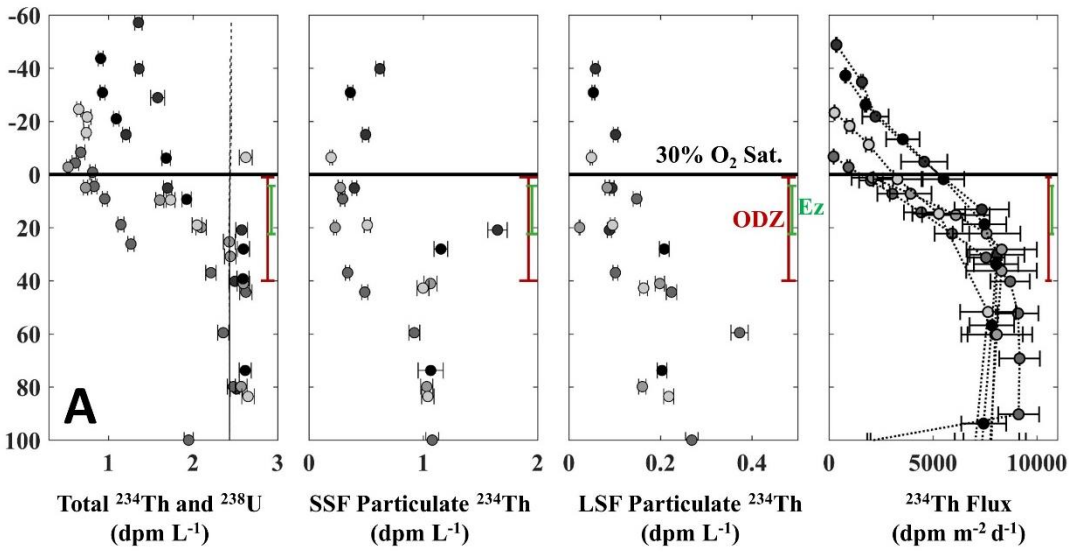

Supplemental Figure 8 (A to E): ^{234}Th results plotted relative to the upper 30% oxygen saturation boundary. Stations are grouped as follows: (A) Shelf Stations 1-5 from 77° W to 80° W, (B) Offshore Stations 6-10 from 80° W to 92° W, (C) Offshore Stations 11-15 from 92° W to 105° W, (D) Gyre Stations 16-26 from 105° W to 129° W, (E) Gyre Stations 27 to 36 from 129° W to 152° W. All data points are shown as depth relative to the surface ocean depth where oxygen saturation levels first reach 30%. This depth is shown as zero (black line). The range in the depth of the euphotic base (Ez) is indicated by the green bracket and the range in the depth of the upper ODZ boundary is indicated by the red bracket. Data shading (filled circles) indicates the location of stations within each region, with black points being the easternmost station and the lightest grey being the westernmost. Note the x-axis change for the ^{234}Th flux panel.

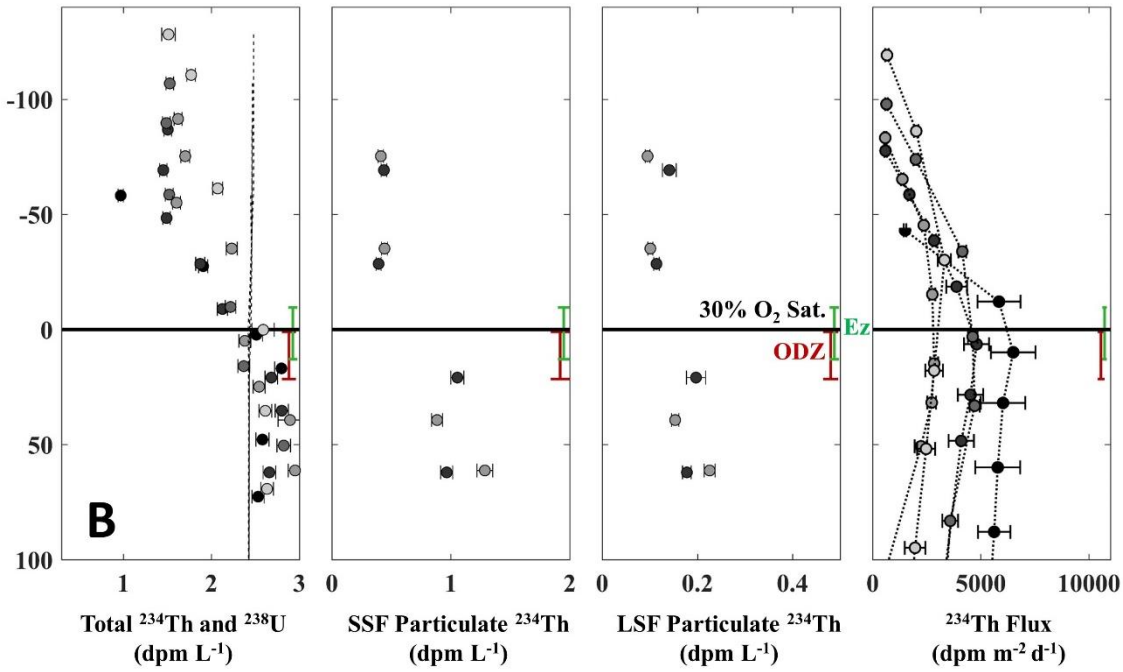

Supplemental Figure 8B: ^{234}Th results plotted relative to the upper 30% oxygen saturation boundary. Details listed with Supp. Fig. 8A.

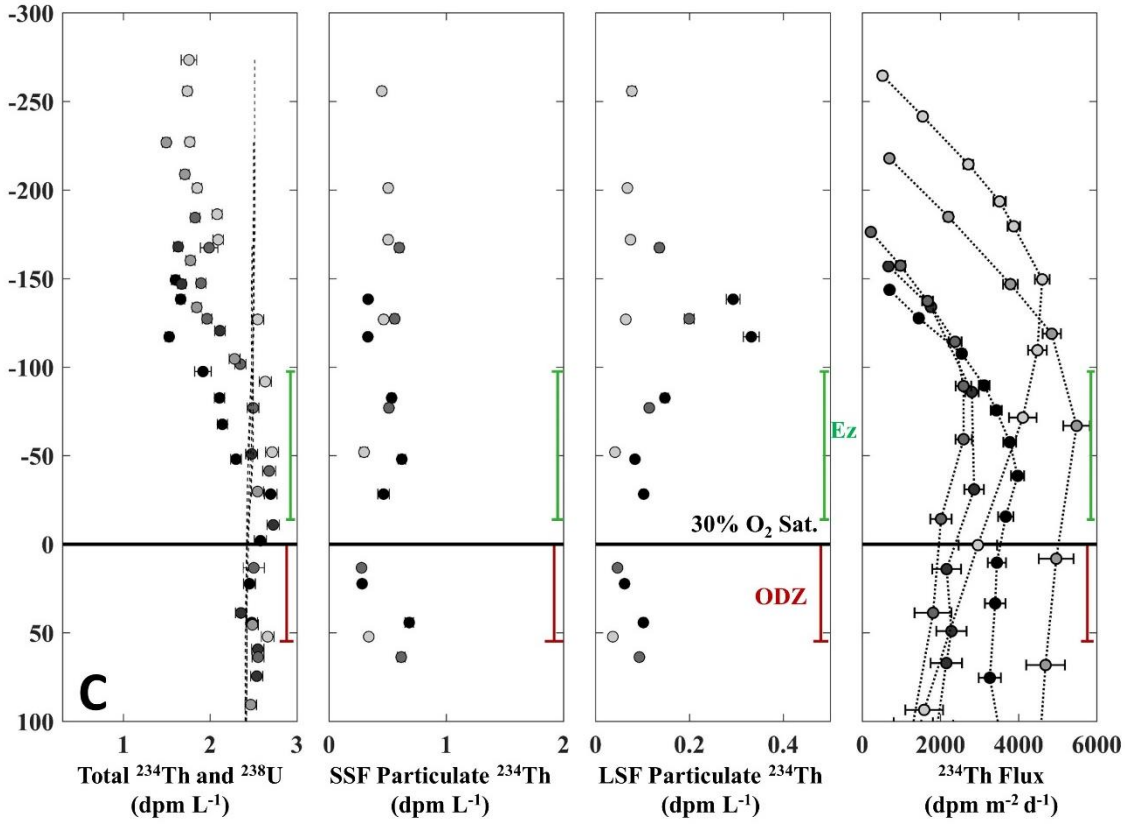

Supplemental Figure 8C: ^{234}Th results plotted relative to the upper 30% oxygen saturation boundary. Details listed with Supp. Fig. 8A.

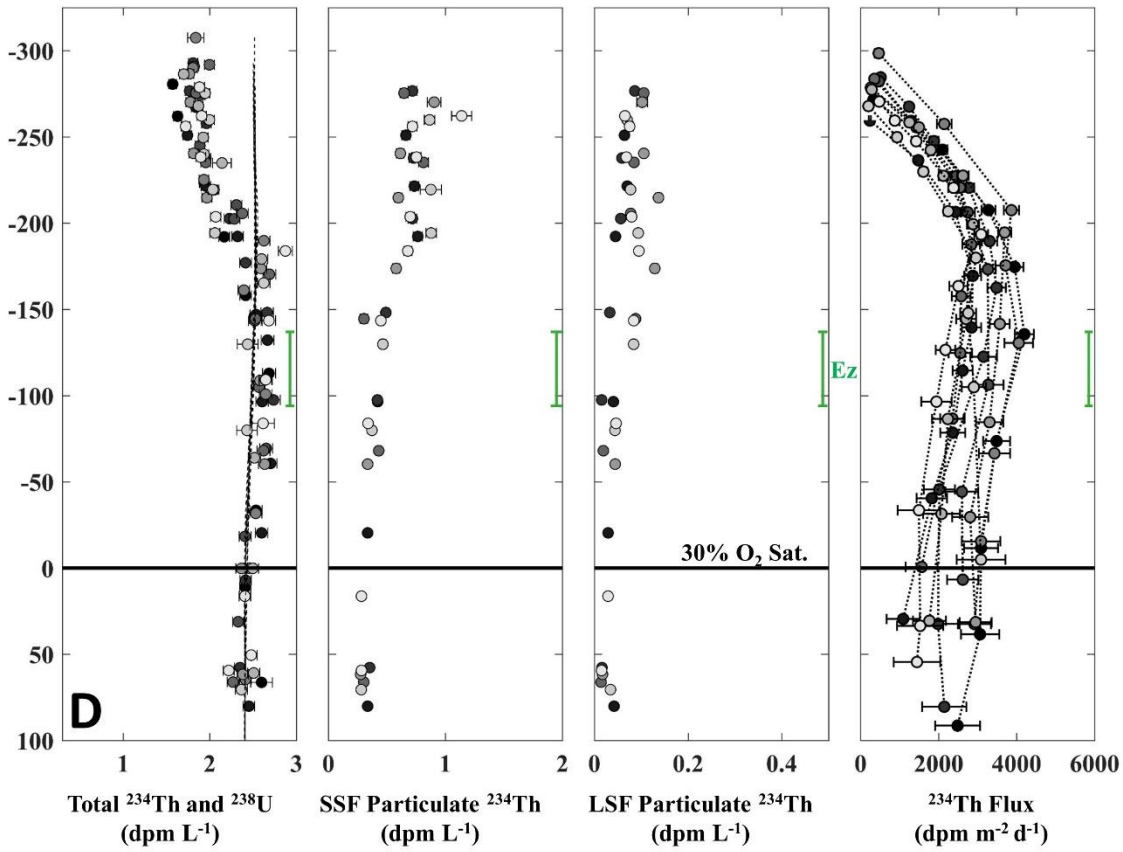

Supplemental Figure 8D: ^{234}Th results plotted relative to the upper 30% oxygen saturation boundary. Details listed with Supp. Fig. 8A.

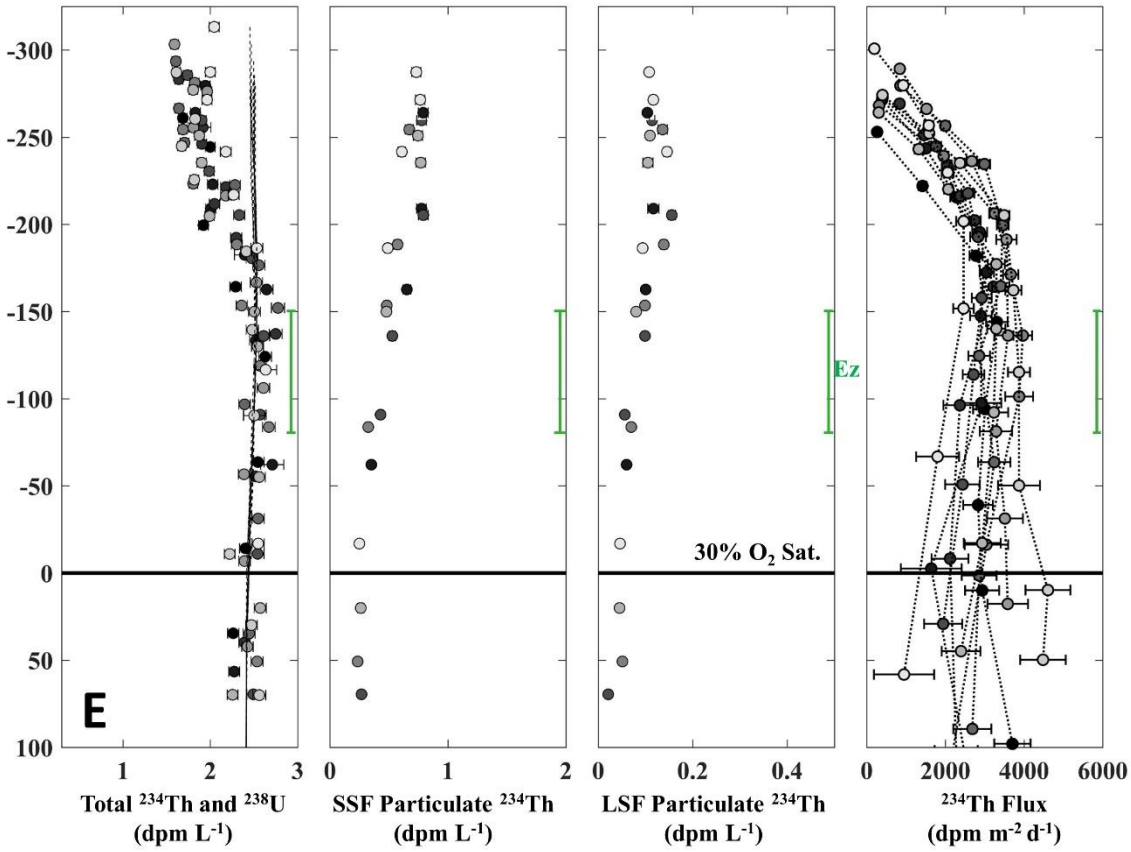

Supplemental Figure 8E: ^{234}Th results plotted relative to the upper 30% oxygen saturation boundary. Details listed with Supp. Fig. 8A.